RSC Sustainability

ROYAL SOCIETY OF CHEMISTRY

TUTORIAL REVIEW

View Article Online
View Journal | View Issue

Check for updates

Cite this: *RSC Sustainability*, 2025, **3**, 2779

Graphene-based catalysts for electrochemical CO_2 reduction reaction

Lankamullage Hasini Amanda Wijewardena,[a] Woo Seok Cheon,[a] Seol-Ha Jeong,*[b] Jungwon Park *[b] and Ho Won Jang *[ac]

Received 9th March 2025
Accepted 5th May 2025

DOI: 10.1039/d5su00174a

rsc.li/rscsus

In response to environmental concerns and the energy transition, electrochemical CO_2 reduction (eCO_2RR) to valuable chemicals and feedstocks using renewable electricity holds significant promise. Yet the challenge remains in developing efficient, low-cost catalysts that exhibit no detrimental environmental effects. Emerging graphene-based materials have demonstrated exceptional potential for eCO_2RR due to their distinctive electronic characteristics and structural advantages, providing remarkable activity, selectivity, and durability. Moreover, they are earth-abundant, non-toxic, and environmentally friendly. This review provides a comprehensive analysis of the application of graphene-based materials as a catalyst for eCO_2RR, focusing on strategies to optimize catalytic performance. Key strategies, such as heteroatom doping and metal-graphene hybridization, are discussed. Furthermore, this review not only explores traditional graphene-based materials but also covers emerging graphene analogs for eCO_2RR. It also highlights challenges, providing perspectives on future research directions to further improve the design and application of graphene-based catalysts for sustainable CO_2 conversion.

Sustainability spotlight

The continuous rise in CO_2 emissions threatens global climate stability, emphasizing the need for carbon-neutral energy solutions. Electrochemical CO_2 reduction offers a sustainable pathway to convert CO_2 into valuable fuels using renewable energy, relying on catalysts to improve efficiency. Conventional catalysts, however, often depend on noble metals or exhibit low efficiency, presenting sustainability challenges. In this regard, graphene-based catalysts offer a sustainable alternative due to their abundance, non-toxicity, and eco-friendliness. With its unique properties, graphene enables more efficient CO_2 reduction, offering environmentally friendly and improved performance. This advancement aligns with UN SDGs 7 (Affordable and Clean Energy), 12 (Responsible Consumption and Production), and 13 (Climate Action), promoting sustainable energy conversion and reducing carbon emissions.

[a]*Department of Materials Science and Engineering, Research Institute of Advanced Materials, Seoul National University, Seoul 08826, Republic of Korea*
[b]*Department of Chemical and Biological Engineering, Seoul National University, Seoul 08826, Republic of Korea. E-mail: jsh528@snu.ac.kr; jungwonpark@snu.ac.kr*
[c]*Advanced Institute of Convergence Technology, Seoul National University, Suwon 16229, Republic of Korea. E-mail: hwjang@snu.ac.kr*

Lankamullage Hasini Amanda Wijewardena

Lankamullage Hasini Amanda Wijewardena is currently a master's degree candidate under the supervision of Prof. Ho Won Jang in the Department of Materials Science and Engineering at Seoul National University. She received her B.S. degree from the Department of Textile and Apparel Engineering at the University of Moratuwa, Sri Lanka, in 2021. Her research interest is focused on the design of metal-graphene-based electrocatalysts for CO_2 reduction.

Woo Seok Cheon

Woo Seok Cheon is currently a PhD candidate under the supervision of Prof. Ho Won Jang at the Department of Materials Science and Engineering of Seoul National University. He received his B.S. degree in the Department of Materials Science and Engineering from Seoul National University in 2021. His research interest is focused on the design of nanostructured metal-based electrocatalysts for CO_2 reduction.

Open Access Article. Published on 07 maí 2025. Downloaded on 23.5.2026 05:53:41.
This article is licensed under a Creative Commons Attribution-NonCommercial 3.0 Unported Licence.

Open Access Article. Published on 07 mai 2025. Downloaded on 23.5.2026 05:53:41.
This article is licensed under a Creative Commons Attribution-NonCommercial 3.0 Unported Licence.

1. Introduction

The sharp rise in atmospheric CO_2 levels, primarily due to fossil fuel combustion and human activities, poses a significant threat to the environment and humankind. This necessitates the urgent need for sustainable solutions to achieve carbon cycle neutrality through the development of advanced carbon recycling technologies. Consequently, various strategies have emerged to reduce fossil fuel dependency and recycle excess CO_2,[1] with carbon capture and storage (CCS) and carbon capture and utilization (CCU) being extensively explored as promising approaches.[2] While CCS is constrained by high costs and associated risks, CCU offers a more sustainable alternative by capturing CO_2 at its source and converting it into fuels and value-added feedstock, thereby addressing both environmental and energy concerns.[3] Among the various strategies within carbon capture and utilization (CCU), eCO_2RR stands out due to its ability to operate under ambient conditions and its potential to generate carbon-based fuels and chemicals from non-fossil fuel energy sources, making it highly aligned with the goals of a sustainable energy economy.[4]

While electrochemical CO_2 reduction (ECR) presents a potential solution for fuel production and the generation of value-added chemicals, the inherent properties of CO_2 pose significant challenges. CO_2 is a highly stable linear molecule with a strong C=O bond (750 kJ mol^{-1}), which poses a challenge for its electrochemical conversion. This strong bond makes CO_2 thermodynamically stable, resulting in a high activation barrier and sluggish conversion. Consequently, significant overpotentials are required to overcome these barriers and drive the reaction.[5] Moreover, ECR becomes more challenging in an aqueous electrolyte due to the multi-proton-coupled electron transfer steps. Furthermore, the competing hydrogen evolution reaction (HER) and the complex reaction pathways

Seol-Ha Jeong

Seol-Ha Jeong is a research professor at the Institute of Chemical Processes, Seoul National University, specializing in bioengineering, tissue engineering, and biomedical devices. She received a B.S. degree (2012), M.S. degree (2014), and PhD (2017) from the department of Materials Science and Engineering at Seoul National University. She has an extensive background, having completed a postdoctoral research position at Seoul National University's Department of Materials Science and Engineering (2018–2022) and worked as a research fellow at Harvard Medical School and Brigham and Women's Hospital (2022–2024). Dr Jeong also served as a senior researcher at the Seoul National University Institute of Biotechnology and the Department of Plastic Surgery at Boramae Medical Center (2024.03–2024.10). Since November 2024, she has joined Professor Jungwon Park's lab at Seoul National University, where she is using in situ liquid-phase transmission electron microscopy to analyze the dynamic structures of biomaterials.

Jungwon Park

Jungwon Park is currently an Associate Professor at Seoul National University, Seoul, Korea. His research field of interest is physical chemistry of nanomaterials and in situ electron microscopy. He started his professional career as an Assistant Professor in the School of Chemical and Biological Engineering at Seoul National University (2016-present), after a postdoc and a research associate position at the School of Engineering and Applied Sciences, Harvard University. He is jointly affiliated in the Center for Nanoparticle Research, Institute for Basic Science, as a Research Associate. He has received various prestigious awards such as Korea Presidential Award for Young Scientists in 2020, The 3rd Hanseong Science Award in 2020, and Wiley-KCS Young Chemist Award in 2021. He serves as an advisory board member for iScience, cell press and an early career advisory board member for ChemNanoMat (Wiley). He received a B.S. degree from the department of Chemistry at POSTECH, Korea in 2003. He then received a PhD from the department of Chemistry at the University of California, Berkeley in 2012.

Ho Won Jang

Ho Won Jang is a full professor at the Department of Materials Science and Engineering of Seoul National University. He received his PhD from the Department of Materials Science and Engineering at Pohang University of Science and Technology in 2004. He worked as a research associate at the University of Wisconsin–Madison from 2006 to 2009. Before he joined Seoul National University in 2012, he had worked at the Korea Institute of Science and Technology (KIST) as a senior research scientist. His research interests include materials synthesis and device fabrication for (photo)electrocatalysis, chemical sensors, memristors, micro-LEDs, and thin film transistors.

© 2025 The Author(s). Published by the Royal Society of Chemistry

Open Access Article. Published on 07 maí 2025. Downloaded on 23.5.2026 05:53:41.
This article is licensed under a Creative Commons Attribution-NonCommercial 3.0 Unported Licence.

leading to a broad range of products make achieving selectivity for a desired product a significant challenge.[6] Therefore, to make CO_2 electrochemical reduction economically viable, electrocatalysts with high selectivity, stability, and activity toward CO_2 are required.[7]

The eCO_2RR has been extensively studied on metal catalysts due to their high catalytic performance. Precious metal-based catalysts such as Au, Ag, and Pt have been well-established for electrochemically converting CO_2 into C1 products with lower overpotentials and high current densities.[8] Yet, they face several challenges, including high costs, scarcity, and negative environmental effects.[9] Moreover, to date, only copper and copper oxide-derived catalysts have been demonstrated to facilitate the electrolysis of CO_2 into hydrocarbons and oxygenates beyond the 2-electron reduction pathway. However, the application of these catalysts is limited by their high overpotential and stability issues,[10] making them inadequate for industrial applications and global commercialization. Therefore, the development of environmentally friendly electrocatalysts with high activity and stability, capable of tuning the competitive reactivity between eCO_2RR and HER, is essential for advancing electrochemical CO_2 reduction.

Graphene-based materials are gaining increasing attention as promising catalysts for ECR due to their unique properties, including a large specific surface area, high electrical conductivity, and exceptional thermal stability.[11] In addition, graphene is a carbon-based material that is abundant and non-toxic and can be synthesized through eco-friendly methods, reducing reliance on scarce or harmful materials.[12] Thus, using graphene-based catalysts for eCO_2RR approaches aims to overcome the intrinsic limitations of metal-based catalysts. Although pristine graphene is relatively inactive for ECR due to its electroneutrality, functionalization induces charge redistribution, enhancing its ability to adsorb and activate CO_2, making it a promising catalyst. For example, heteroatom-doped metal-free graphene-based catalysts have shown promising results in eCO_2RR, producing CO with faradaic efficiencies (FE) exceeding 90% at low overpotentials, rivaling those of silver and gold.[13–17] Moreover, metal-graphene hybridized catalysts have achieved FEs for C_2 products as high as 90% at overpotentials comparable to copper.[18,19] Hence, advancements in graphene-based catalysts will be pivotal for driving sustainable energy conversion technologies.

This paper provides a comprehensive review of recent progress on graphene-based materials for the electrocatalytic conversion of CO_2 into value-added products. We first present an overview of eCO_2RR, including evaluation parameters and characterization techniques. Next, a systematic review of the role of graphene-based materials, along with their optimization strategies such as metal-free heteroatom doping and metal hybridization, is provided, along with the application of these materials for the electrochemical conversion of CO_2. Following that, the advances in emerging graphene analogs as an extension of graphene-based catalysts for eCO_2RR are presented. A schematic overview of the major categories of graphene-based catalysts explored for eCO_2RR is illustrated in Fig. 1. Finally, an outlook on the future development of graphene-based catalysts and electrochemical systems for eCO_2RR is discussed.

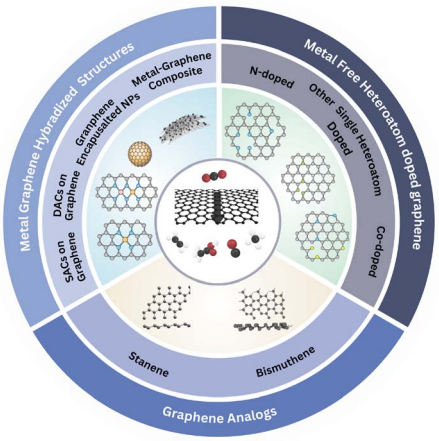

Fig. 1 Schematic representation categorizing graphene-based catalysts designed for eCO_2RR.

2. Key aspects of eCO_2RR

2.1 Fundamentals of eCO_2RR

CO_2, with an oxidation state of +4, represents the highest oxidation state of carbon. Consequently, converting CO_2 into a more energetic product necessitates the transfer of electrons to carbon, lowering its oxidation state.[5] The conversion of CO_2 into more reduced products is referred to as CO_2 reduction, with eCO_2RR specifically referring to the use of electrical energy to drive this transformation into various carbon-based products. Generally, this process is performed in an electrolyzer consisting of a cathode and an anode separated by an electrolyte. The electrode is solid for heterogeneous catalysts, and the electrolyte is an aqueous solution saturated with CO_2. The electrolysis process typically occurs at the electrode–electrolyte interface. During the eCO_2RR process, the cathode facilitates the reduction of carbon dioxide into useful hydrocarbons, aldehydes, or alcohols, while the anode undergoes the oxygen evolution reaction (OER), producing oxygen to complete the overall reaction. The reaction mechanisms are outlined below.[20]

At the cathode

$$xCO_2 + nH^+ + ne^- \rightarrow \text{product} + yH_2O \quad (1)$$

At the anode,

$$2H_2O \rightarrow O_2 + 4H^+ + 4e^- \quad (2)$$

Mechanistically, three principal steps are involved in the conversion of CO_2 into carbon-based products.[21] The first step involves the adsorption and activation of CO_2 onto the electrode surface. This is followed by proton-coupled electron transfer (PCET) processes that generate various products through different reaction pathways involving 2 to 8 electrons. Finally,

Open Access Article. Published on 07 mai 2025. Downloaded on 23.5.2026 05:53:41.
This article is licensed under a Creative Commons Attribution-NonCommercial 3.0 Unported Licence.

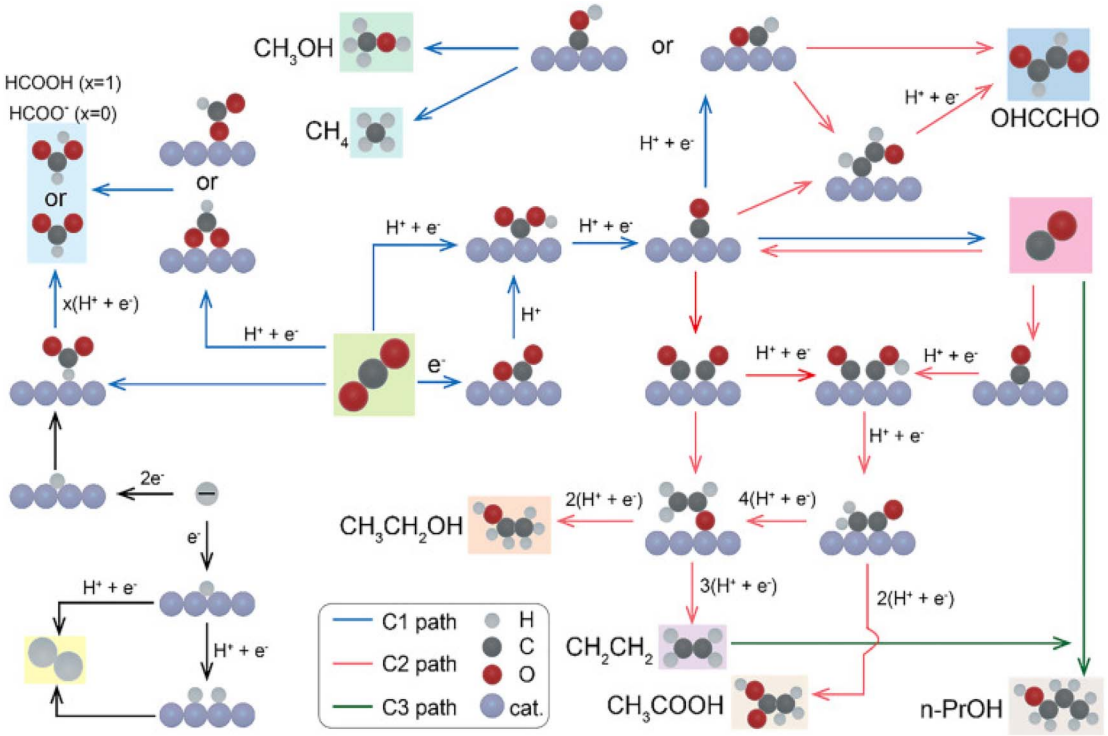

Fig. 2 Mechanistic pathways for electrochemical CO_2 reduction to C_1, C_2, and C_3 products. Adapted with permission from ref. 22 Copyright 2023, Elsevier.

the products desorb from the catalyst surface and diffuse into the electrolyte. The final product distribution is highly dependent on the properties of the electrocatalyst and the applied electrode potential. A diverse range of products can be obtained, including C_1 compounds such as carbon monoxide (CO), formic acid (HCOOH), methanol (CH_3OH), formaldehyde (HCHO), and methane (CH_4), as well as C_{2+} products like ethylene (CH_2CH_2), ethanol (C_2H_5OH), and acetate (CH_3COOH). As illustrated in Fig. 2, the formation of CO and HCOOH is relatively straightforward, each involving only a single pathway.[22] In contrast, methane and methanol may proceed through either the $*CH_2OH$ or $*OCH_3$ intermediate, while the formation of C_{2+} products involves multiple intermediates, making product selectivity more complex. For example, acetate can be formed *via* hydrogenation of *CO to $*CH_2$, which then reacts with CO to form $*CH_2CO$, or alternatively through *CO dimerization to *COCHO followed by hydrogenation.[23] Ethanol and ethylene share the intermediate $*CH_2CHO$, with ethanol forming *via* further PCET steps, while ethylene results from dehydration.[24] Ethane forms through sequential PCET on CO to generate CH_3, which then couples to yield ethane. Ethylene glycol synthesis starts from *CHO formation, followed by CO insertion and multiple PCET steps.[25] Table 1 summarizes the half-reactions and their equilibrium potentials relative to the standard hydrogen electrode (SHE) at pH 7.

Steering the selectivity of catalysts towards specific products in eCO_2RR is challenging due to the wide range of possible carbon-based outputs. Pioneering work by Hori *et al.*[26] classified metal catalysts based on their FE and the types of products they generate, showing that different metals tend to produce specific products such as H_2, HCOOH, CO, or more complex hydrocarbons, depending on their catalytic properties.[27] According to the Sabatier principle, optimal catalytic performance requires a balanced interaction between the catalyst and reaction intermediates, neither too weak nor too strong, to ensure effective adsorption and product release, which explains the performance differences among various metal catalysts.

Table 1 The potential half-reactions occurring at the cathode during CO_2 electrochemical reduction, along with their equilibrium potentials *versus* the Standard Hydrogen Electrode (SHE) in a pH 7 electrolyte[7]

CO_2 reduction half-reaction	E^0 [V *vs.* SHE]
$CO_2 + 2H^+ + 2e^- \rightarrow HCOOH + H_2O$	$E_{redox}^0 = -0.610$ V
$CO_2 + 2H^+ + 2e^- \rightarrow CO + H_2O$	$E_{redox}^0 = -0.530$ V
$2CO_2 + 2H^+ + 2e^- \rightarrow H_2C_2O_4$	$E_{redox}^0 = -0.913$ V
$CO_2 + 4H^+ + 4e^- \rightarrow HCHO + H_2O$	$E_{redox}^0 = -0.480$ V
$CO_2 + 6H^+ + 6e^- \rightarrow CH_3OH + H_2O$	$E_{redox}^0 = -0.380$ V
$CO_2 + 8H^+ + 8e^- \rightarrow CH_4 + 2H_2O$	$E_{redox}^0 = -0.240$ V
$2CO_2 + 12H^+ + 12e^- \rightarrow C_2H_4 + 4H_2O$	$E_{redox}^0 = -0.349$ V
$2CO_2 + 12H^+ + 12e^- \rightarrow C_2H_5OH + 3H_2O$	$E_{redox}^0 = -0.329$ V
$2CO_2 + 14H^+ + 14e^- \rightarrow C_2H_6 + 4H_2O$	$E_{redox}^0 = -0.270$ V
$3CO_2 + 18H^+ + 18e^- \rightarrow C_3H_7OH + H_2O$	$E_{redox}^0 = -0.310$ V
$2H^+ + 2e^- \rightarrow H_2$	$E_{redox}^0 = -0.42$ V

2.2 Evaluation parameters

2.2.1 Onset potential. The onset potential is the applied potential *versus* the reference electrode at which a detectable

© 2025 The Author(s). Published by the Royal Society of Chemistry

Open Access Article. Published on 07 maí 2025. Downloaded on 23.5.2026 05:53:41.
This article is licensed under a Creative Commons Attribution-NonCommercial 3.0 Unported Licence.

current corresponding to the desired product yield begins. It indicates the ease of initiating a reaction on the catalyst. During the eCO_2RR, a less negative onset potential indicates a more efficient catalyst, whereas a more negative onset suggests a higher energy requirement.

2.2.2 Overpotential. Overpotential refers to the additional voltage required beyond the thermodynamic equilibrium potential to drive the electrochemical reaction at a desired rate. In eCO_2RR, the overpotential reflects the energy barrier that must be overcome for the reaction to proceed effectively. It is influenced by factors such as catalyst material, surface morphology, and reaction conditions.

2.2.3 Faradaic efficiency. The faradaic efficiency represents the ratio of the charge utilized for the desired electrochemical reaction to the total charge passed through the system. This indicates how effectively the electrons contribute to the formation of specific products.

2.2.4 Tafel slope. The Tafel slope, a key kinetic parameter in electrochemical studies, represents the relationship between the overpotential and the logarithm of the current density. A smaller Tafel slope indicates better catalytic performance, while a larger slope suggests a more complex mechanism.

2.2.5 Stability. Stability is a critical parameter for evaluating the practical application of catalysts. It can be measured using two methods, voltammetric (CV or LSV) and galvanostatic/potentiostatic electrolysis. In the voltammetric method, overpotential changes are compared before and after cycling (*e.g.*, 10 000 cycles), with minimal change indicating stability. The galvanostatic/potentiostatic approach monitors potential or current density over time at a constant current density ($\geq$10 mA cm^{-2}) for at least 10 hours, where minimal variation signifies good stability.

2.2.6. Single-pass conversion efficiency (SPCE). SPCE is a key performance benchmark for chemical processes. In eCO_2RR, SPCE is defined as the ratio of the amount of CO_2 converted to the total amount of CO_2 entering the electrolyzer in a single pass.

3 Graphene-based materials as a catalyst for eCO_2RR

3.1 Properties of graphene-based materials

Since its discovery by Novoselov and Geim in 2004, graphene has been the focus of research due to its unique properties, such as exceptionally high surface area, outstanding conductivity, and excellent thermal and chemical stability.[28,29] This single-atom-thick carbon structure is not only easy to modify into various structures, such as graphene oxide (GO), reduced graphene oxide (rGO), and carbon nanotubes (CNTs), but also versatile in assembling into various allotropes- (0D) fullerenes, (1D) nanotubes, (2D) graphene, or (3D) stacked-graphene (Fig. 3),[30–32] while retaining the two-dimensional hexagonal lattice of sp^2-hybridized carbon atoms as their fundamental building block.[33] This structural diversity of graphene has laid the basis for developing novel graphene-based catalysts, which have attracted increasing interest for applications in electrocatalytic energy conversion. However, pristine graphene and its derivatives exhibit limited catalytic performance for some electrochemical reactions including eCO_2RR due to their highly ordered and inert carbon structure. This results in poor adsorption and activation of CO_2 molecules during the eCO_2RR. This provides greater flexibility for modifications to optimize the catalytic properties of graphene-based materials. The introduction of non-metal heteroatoms and metal hybrid

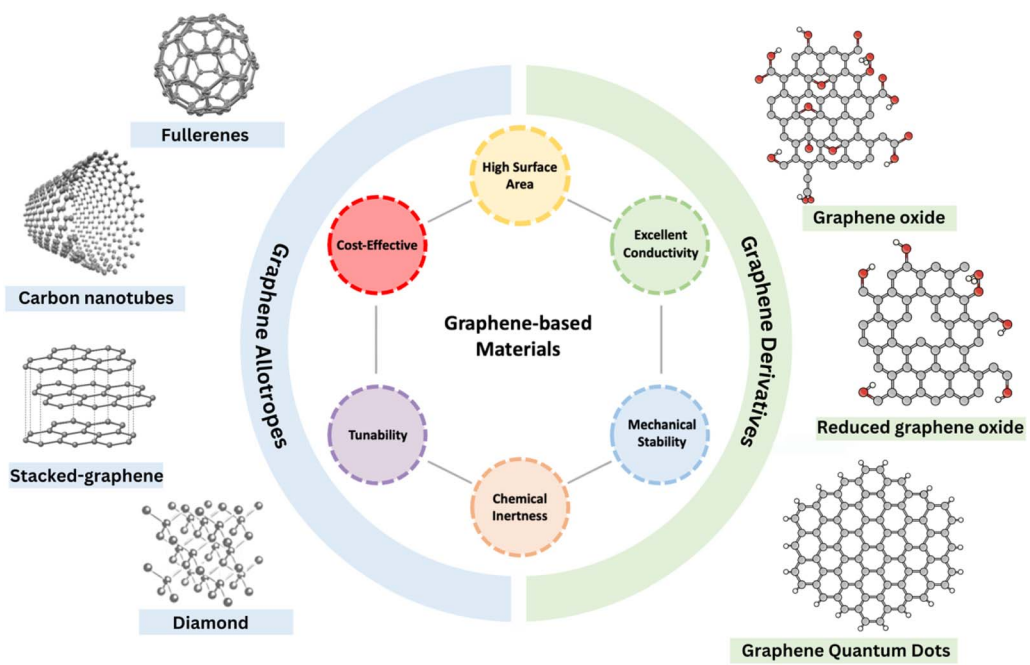

Fig. 3 Schematic representation of graphene-based materials, including graphene allotropes and derivatives, highlighting their key properties.

Open Access Article. Published on 07 maí 2025. Downloaded on 23.5.2026 05:53:41.
This article is licensed under a Creative Commons Attribution-NonCommercial 3.0 Unported Licence.

formation with non-noble metals has been utilized to enhance the catalytic performance of graphene.

3.2 Graphene-based catalyst optimization strategies: a classification approach

Graphene-based catalysts can be broadly divided into three main categories based on their compositional structure, offering distinct optimization strategies for enhancing eCO_2RR performance. First, metal-free heteroatom-doped graphene utilizes non-metallic dopants to introduce active sites within the graphene lattice. Second, metal–graphene hybrids combine single atoms or metal nanoparticles with graphene to utilize the synergistic effects between the metal components and the conductive carbon support. Third, graphene analogues, including materials such as bismuthene and stanene, possess graphene-like two-dimensional structures but are composed of different elements, offering unique catalytic properties.

3.2.1 Metal-free heteroatom doping. Heteroatom doping is an effective strategy to enhance the electrocatalytic performance of graphene-based materials by modulating their electronic properties and generating active sites. Various elements, including P-block, such as sulfur, nitrogen, boron, and phosphorus, have been reported for graphene doping.[34] Doping graphene with these heteroatoms alters its structure and properties due to the charge distribution changes and structural defects, allowing graphene to be employed as an active center of eCO_2RR.[35] For example, when the electronegativity of a heteroatom differs from that of carbon atoms, doping disrupts the symmetry of the sp^2 carbon network and alters the charge distribution in graphene. This results in an uneven charge distribution at the adjacent carbon atom positions, enhancing the adsorption of CO_2 and intermediates, thereby facilitating electron transfer to the adsorbed molecules. In addition, these charge distribution changes also shift the Fermi level and open the band gap, optimizing electron transfer and improving catalytic efficiency. Conversely, when the electronegativity is similar, but the covalent radius differs, local structural changes occur, leading to increased asymmetric spin density and the creation of catalytically active sites.[36]

Single heteroatom doping involves the incorporation of one type of heteroatom into the graphene lattice. Among these, nitrogen doping is the most widely studied and highly effective method for enhancing catalytic properties in graphene-based materials. This is due to nitrogen's similar atomic size to carbon and its strong electron-donating ability, which facilitates seamless integration into the graphene structure and creates active sites for catalytic reactions. As presented schematically in Fig. 4a, nitrogen can exist in various N species, including pyridinic-N, pyrrolic-N, graphitic-N, and pyrazole-N.[37] Pyridinic nitrogen is sp^2-hybridized, substitutes a carbon atom within the hexagonal lattice, and donates a single p-electron to the π-electron system. Pyrrolic nitrogen, which is sp^3-hybridized, replaces a carbon atom in a five-membered ring and provides two p-electrons to the π-electron system. Graphitic nitrogen, being sp^2-hybridized, substitutes a carbon atom within the hexagonal lattice. These N-species have significantly varying impacts on the carrier concentration, leading to distinct electronic structures in the N-doped graphene.[38] Recently, much work has been dedicated to unveiling the origin of activity from nitrogen doping in the eCO_2RR. DFT calculations indicate that the nitrogen atom of pyridine can form a hydrogen bond with the hydrogen atom of the important intermediate *COOH, therefore decreasing the reaction's free energy and stabilizing the key intermediate. Furthermore, both graphitic and pyridinic nitrogen have been reported to initiate catalytic activity for the process. Due to the complexity of many N dopants influencing activity, the active sites for CO_2 reduction on N-doped graphene-based materials are still under debate.[39]

Single heteroatom doping also includes the incorporation of other non-metallic elements such as boron, sulphur, and phosphorus into the graphene lattice. Although less studied than nitrogen, these dopants also play important roles in enhancing catalytic performance by altering the local electronic structure and inducing charge redistribution. Their different electronegativity and atomic sizes compared to carbon create unique active sites that promote CO_2 adsorption and conversion through distinct mechanisms. Due to the lower electronegativity of boron compared to carbon, boron doping in graphene generates electron deficiency in the carbon atoms, resulting in a noticeable difference in electron densities across the graphene structure. As shown in Fig. 4b,[35] the XPS B1s spectrum displays two peaks, indicating that boron atoms in the graphene network have two bonding types: a smaller peak at 198.5 eV for boron silane in the π-conjugated system, and a stronger peak at 200.5 eV for graphitic boron, suggesting substitutional doping of boron into the graphene lattice. Due to the relatively higher electropositivity of B compared to C atoms, B-doping generates charge imbalances in the carbon structure, which helps stabilize the negatively charged oxygen atoms of CO_2, thus promoting stronger chemisorption of CO_2 to the carbon surface during the eCO_2RR process.[40] In comparison, sulphur, with an electronegativity of 2.58, is almost identical to carbon, which has an electronegativity of 2.55, resulting in minimal charge density distribution effects in S-doped graphene. The interaction between sulphur 3p and carbon 2p orbitals, which induces sp^3 hybridization, creating a tetrahedral-like distortion with neighbouring carbon atoms, leads to an uneven spin density, imparting graphene catalytic properties.[41] As presented in Fig. 4c, S dopant atoms can be observed on the S-doped graphene through the adsorption of S onto the graphene surface, the replacement of C by S at the edges, the creation of S/S oxide at the edges, and an S-containing ring linking two graphene sheets.[42] Due to the larger atomic radius of sulphur (1.04 Å) compared to carbon (0.77 Å), S atoms tend to incorporate at the edges of graphene.

In addition to single-atom doping, co-doping strategies involve the simultaneous incorporation of two different heteroatoms into the graphene lattice. These heteroatoms, such as nitrogen and sulphur, nitrogen and phosphorus, or boron and nitrogen, work together to combine their unique electronic and structural effects. Co-doping allows for the optimization of multiple properties at once, leading to synergistic enhancements in charge distribution, active site formation, and the

© 2025 The Author(s). Published by the Royal Society of Chemistry

Open Access Article. Published on 07 maí 2025. Downloaded on 23.5.2026 05:53:41.
This article is licensed under a Creative Commons Attribution-NonCommercial 3.0 Unported Licence.

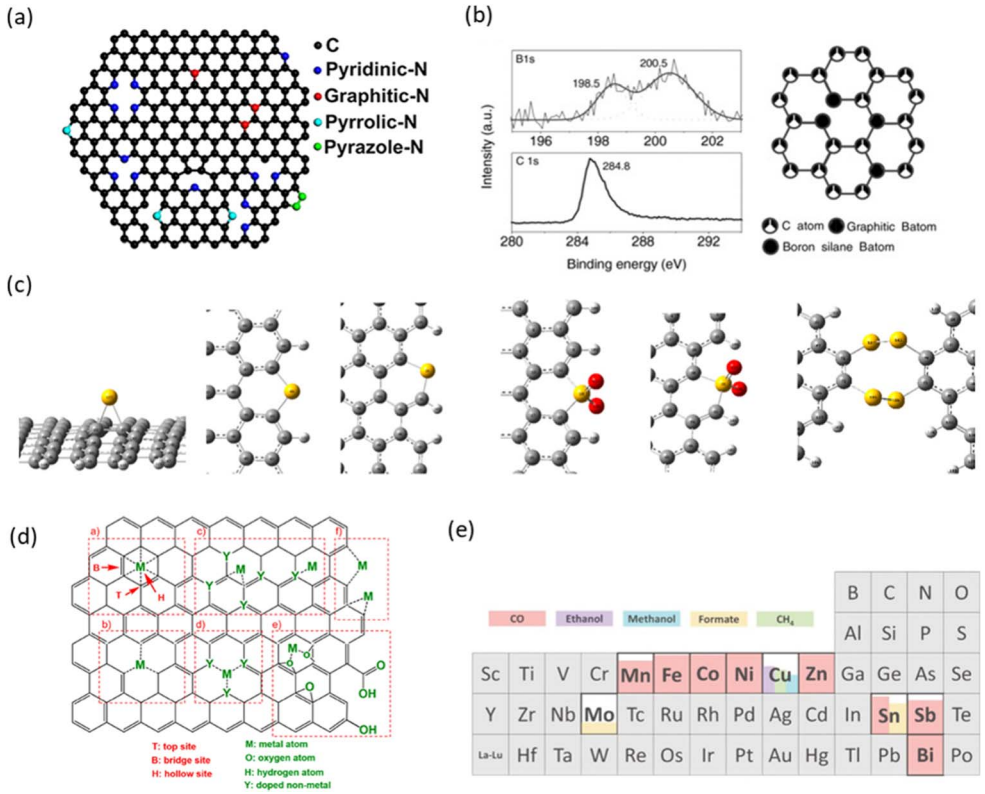

Fig. 4 (a) Structural configurations of N-doped graphene. Adapted with permission from ref. 37 Copyright 2016, Springer Nature. (b) XPS spectra (B1s and C1s) of B-doped graphene. Adapted with permission from ref. 35 Copyright 2012, Wiley. (c) Potential structures of S-doped graphene. Adapted with permission from ref. 42 Copyright 2014, American Chemical Society. (d) Binding modes of metal single atoms on graphene. Adapted with permission from ref. 55 Copyright 2020, American Chemical Society. (e) Summary of reported active elements in SACs for eCO_2RR. Adapted with permission from ref. 56 Copyright 2020, Wiley.

adsorption of key intermediates. This often results in improved catalytic activity, increased selectivity for specific products, and enhanced stability in eCO_2RR.

3.2.2 Metal hybridization. In addition to serving as an active center, graphene can play a critical role in electrochemical reactions by forming metal hybrids, providing structural and electronic benefits without directly participating in the reaction itself. Various forms of graphene-based materials, ranging from zero to three-dimensional structures, have been explored to design and synthesize these hybrids to enhance the electrocatalytic performance of metals.[43–46] The synergy between these combined structures enhances the catalytic activity of metals, surpassing the capabilities of the individual components.

These metal-graphene hybrids can be classified into four key configurations based on the form and the scale of metal integration. One configuration involves isolated single metal atoms anchored onto graphene, forming single-atom graphene systems that maximize atomic utilization and provide well-defined active sites. Another configuration features paired metal atoms coordinated on the graphene lattice, creating dual-atom graphene systems that enable unique electronic interactions and synergistic effects. In contrast, fully encapsulated metal nanoparticles, covered by graphene layers, form metal-encapsulated systems, where the graphene shell provides stability while allowing selective access to the active metal core. Lastly, metal nanoparticles or clusters supported on graphene constitute metal-graphene composites, combining the advantages of nanoscale metals with graphene's conductive framework. This structural classification emphasizes how varying degrees of metal-graphene integration influence catalytic behavior, from single-site precision to multifunctional architectures.

Graphene has been effectively utilized as a particle stabilizer for single atoms and dual atoms in eCO_2RR. Its exceptional two-dimensional structure and high specific surface area help anchor these active centers, preventing agglomeration during electrochemical processes.[47] Moreover, the surface of graphene can be modified with various functional groups, including those containing nitrogen and oxygen.[48] These functional groups enhance graphene's ability to stabilize metal species by serving as anchoring sites for single atoms and metal nanoparticles, preventing their migration or aggregation.[49] As a result, graphene serves as an ideal substrate for loading metal atoms, substantially improving their dispersion, stability, and electrocatalytic performance, ultimately contributing to enhanced reaction efficiency. Fig. 4d illustrates the various binding sites for single atoms (SAs) on graphene, including pristine graphene,[50] defective graphene with vacancies,[51] doped graphene,[52] and edge sites.[53,54] These binding modes differ in

Open Access Article. Published on 07 mai 2025. Downloaded on 23.5.2026 05:53:41.
This article is licensed under a Creative Commons Attribution-NonCommercial 3.0 Unported Licence.

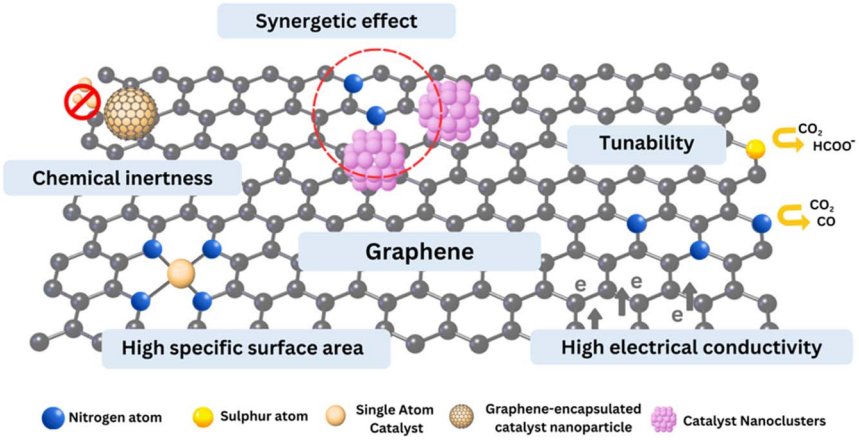

Fig. 5 Schematic representation of the advantages of graphene-based catalysts for electrochemical CO_2 Reduction.

stability and efficiency, with defective and doped graphene generally enhancing the stability of metal SAs.[55] The efficiency and selectivity of SAs for eCO_2RR vary depending on their elemental properties and group number in the periodic table, as shown in Fig. 4e.[56]

Graphene can also serve as a protective cover for the active phase, such as metal catalysts, in eCO_2RR. exceptional mechanical strength and impermeability prevent corrosion and oxidation of the underlying active material, ensuring long-term stability. Additionally, graphene's chemical inertness under reaction conditions preserves the catalyst's integrity, while its ability to modulate local environments, such as the concentration of reactants, further enhances the selectivity and efficiency of the reaction.

In the form of metal-graphene composite structures, graphene acts as a conductive matrix that supports and enhances the activity of metal catalysts in eCO_2RR due to the excellent electrical conductivity (1×10^5 S m^{-1}) of graphene.[57,58] Therefore, graphene can serve as an ideal conductor, significantly improving the electrical conductivity of the hybrid catalyst composites. Its excellent electrical conductivity facilitates efficient electron transfer, while its mechanical strength ensures enhanced stability under reaction conditions. The synergy between the combined structures also promotes easy adsorption of CO_2 on the catalyst surface.[59]

3.2.3. Graphene analogs. Emerging graphene analogs, particularly 2D monoelemental materials (*e.g.*, bismuthene, stanene, phosphorene), have gained significant attention as electrocatalysts for CO_2 reduction due to their unique electronic properties, high surface-to-volume ratio, and tunable catalytic activity.[60] Unlike conventional graphene, these materials exhibit intrinsic metallic or semiconducting behavior, anisotropic charge transport, and abundant active sites, making them promising candidates for the eCO_2RR.[61] For instance, bismuthene demonstrates high selectivity for formate production due to its partially occupied p-orbitals, which facilitate CO_2 activation and stabilization of the OCHO intermediate.[62] The catalytic performance of these materials can be further enhanced through defect engineering, strain modulation, or heteroatom doping, which tailor their electronic structure and surface reactivity.[63] Moreover, the quantum confinement effect in 2D monoelemental materials leads to discrete energy levels, enabling precise tuning of their Fermi level and bandgap for optimal charge transfer during eCO_2RR.[64] These materials also exhibit superior stability under electrochemical conditions compared to traditional metal-based catalysts, addressing a critical challenge in CO_2 electroreduction.[65]

To outline the concepts discussed above, a schematic overview is presented in Fig. 5, illustrating the key advantages of graphene-based materials in electrochemical CO_2 reduction.

4. Characterization of graphene-based catalysts

The characterization of graphene-based catalysts for eCO_2RR requires a comprehensive analysis of the intrinsic properties, such as surface morphology, defect density, and electronic structure, as well as the electrochemical reaction mechanisms, to enhance the catalytic performance. The most commonly used methods for characterizing graphene-based catalysts in electrochemical CO_2 reduction can be divided into two categories: *ex situ* and *in situ* techniques. *Ex situ* characterization involves analyzing the catalyst before or after the electrochemical reaction, providing detailed information about its structural, morphological, and compositional properties. *In situ* characterization, on the other hand, focuses on real-time monitoring of the catalyst's behavior under electrochemical conditions. This approach provides crucial insights into the reaction intermediates, active sites, and dynamic changes in the catalyst's electronic structure during eCO_2RR.[66]

4.1 *Ex situ* characterization

Methods such as scanning electron microscopy (SEM) transmission electron microscopy (TEM), and high-angle annular dark-field scanning transmission electron microscopy (HAADF-STEM) are commonly used to analyze the morphology and structure of graphene-based catalysts, offering detailed images

© 2025 The Author(s). Published by the Royal Society of Chemistry

Open Access Article. Published on 07 maí 2025. Downloaded on 23.5.2026 05:53:41.
This article is licensed under a Creative Commons Attribution-NonCommercial 3.0 Unported Licence.

of surface topography, layer thickness, defect sites, and the arrangement of metal nanoparticles or single atoms on the graphene substrate as shown in Fig. 6a and b.[67] In addition, changes in catalyst morphology during electrochemical reactions, both before and after the CO_2RR, can be revealed, providing insights into the structural evolution, stability, and potential aggregation of nanoparticles as presented in Fig. 6c and d.[68] The crystallinity and phase composition can be characterized using X-ray diffraction (XRD) and selected area electron diffraction (SAED). As depicted in Fig. 6e, the XRD measurement confirms the successful oxidation, functionalization, and doping of graphene were achieved, as evidenced by shifts in diffraction peaks and changes in peak intensities.[69] The degree of structural deformation of catalysts can be

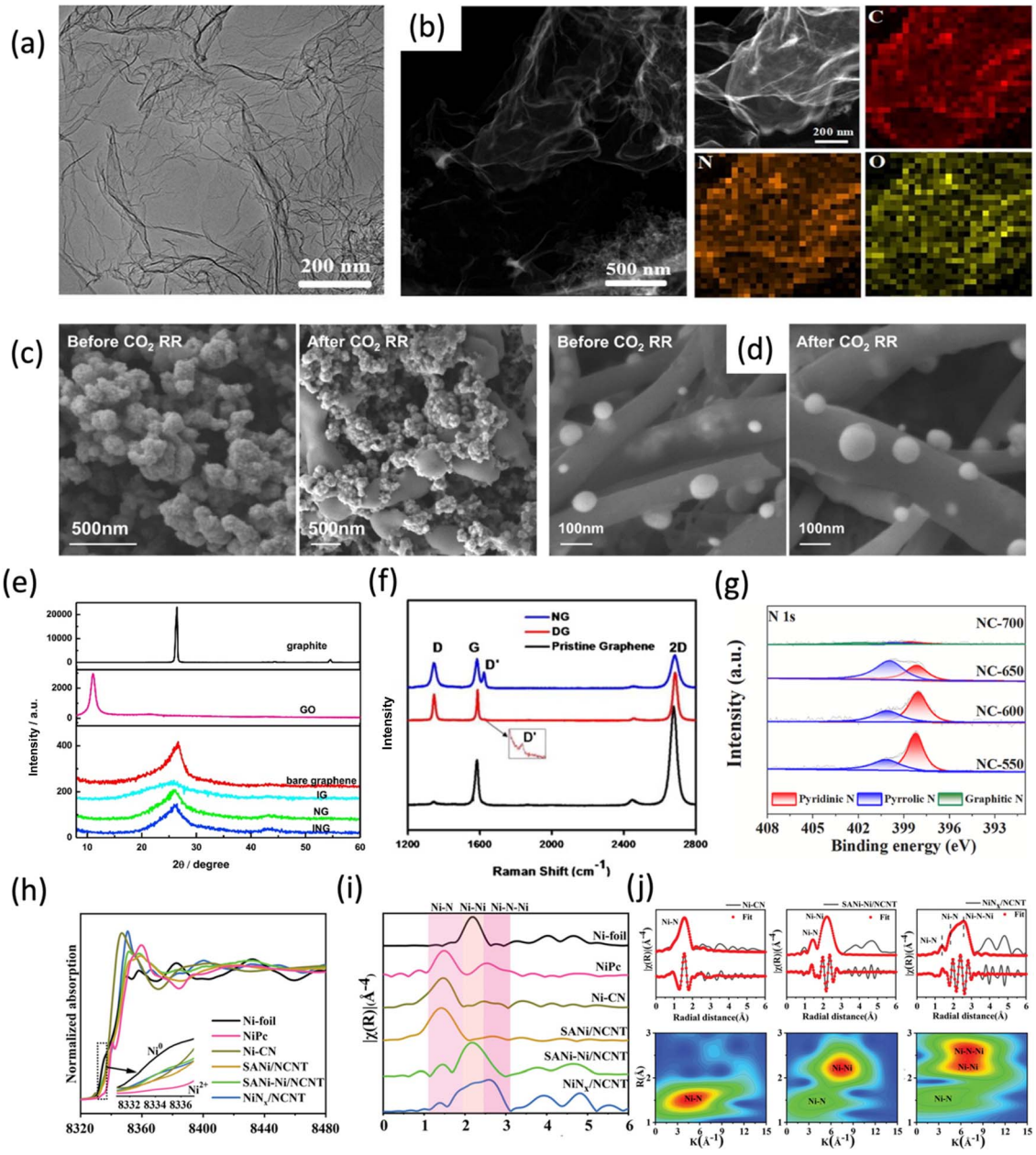

Fig. 6 *Ex situ* characterization (a) TEM (b) HAADF-STEM elemental mapping images of N-doped graphene (NG-1000). Adapted with permission from ref. 67 Copyright 2021, Elsevier. (c) Unconfined and (d) confined Cu nanoparticles before and after the eCO_2RR, respectively. Adapted with permission from ref. 68 Copyright 2021, Springer Nature (e) XRD patterns of graphite, GO, bare graphene, iodine-doped graphene (IG), NG, and I and N co-doped graphene (ING). Adapted with permission from ref. 69 Copyright 2015, Elsevier. (f) Raman spectra of pristine graphene, defective graphene (DG) and NG. Adapted with permission from ref. 70 Copyright 2013, Elsevier. (g) High-resolution N1s XPS spectra of carbon. Adapted with permission from ref. 71 Copyright 2023, Elsevier. (h) Structural characterization of nickel-based catalysts using Ni K-edge XANES spectra. (i) Fourier transform k^3-weighted R-space χ EXAFS spectra for Ni–CN, NiSA/NCNT, SANi-Ni/NCNT, NiN_x/NCNT, and reference materials (NiPc and Ni foil). (j) EXAFS fitting and wavelet transforms of Ni K-edge EXAFS signals for Ni–CN, SANi-Ni/NCNT, and NiN_x/NCNT. Adapted with permission from ref. 73 Copyright 2023, Wiley.

© 2025 The Author(s). Published by the Royal Society of Chemistry

Open Access Article. Published on 07 mai 2025. Downloaded on 23.5.2026 05:53:41.
This article is licensed under a Creative Commons Attribution-NonCommercial 3.0 Unported Licence.

assessed using Raman spectra, as demonstrated in Fig. 6f. Raman analysis of pristine, defective, and doped graphene reveals that the pristine graphene shows strong G and 2D bands, while defective graphene, such as nitrogen-doped, exhibits an additional D band. Increased D/G intensity ratios indicate a higher density of defects due to substitutions, vacancies, and structural disruptions, thus providing insights into the defect concentration and doping level in the graphene structure.[70] Additionally, as illustrated in Fig. 6g, the X-ray photoelectron spectroscopy (XPS), analysis of the N1s spectra allows for the identification of the incorporation of nitrogen into the carbon structure and the formation of various nitrogen bonding types.[71] As shown in Fig. 6h and i, the synchrotron-radiation-based X-ray absorption fine structure (XAFS), including both X-ray absorption near-edge structure (XANES) and extended X-ray absorption fine structure (EXAFS), can be used to examine the coordination environment and electronic states of metal species in catalysts.[72] XANES analysis offers insight into the oxidation states of metal species while the EXAFS analysis helps identify the coordination environment and differentiate between single-atom catalysts and metallic clusters. Additionally, the wavelet transform (WT) of EXAFS (Fig. 6j) signals offers a more detailed view of the coordination environment and bonding interactions in the catalyst.[73]

4.2 *In situ* characterization

The *in situ*/*operando* TEM technique enables real-time characterization of catalyst morphology changes during reactions through imaging and diffraction techniques by applying light,

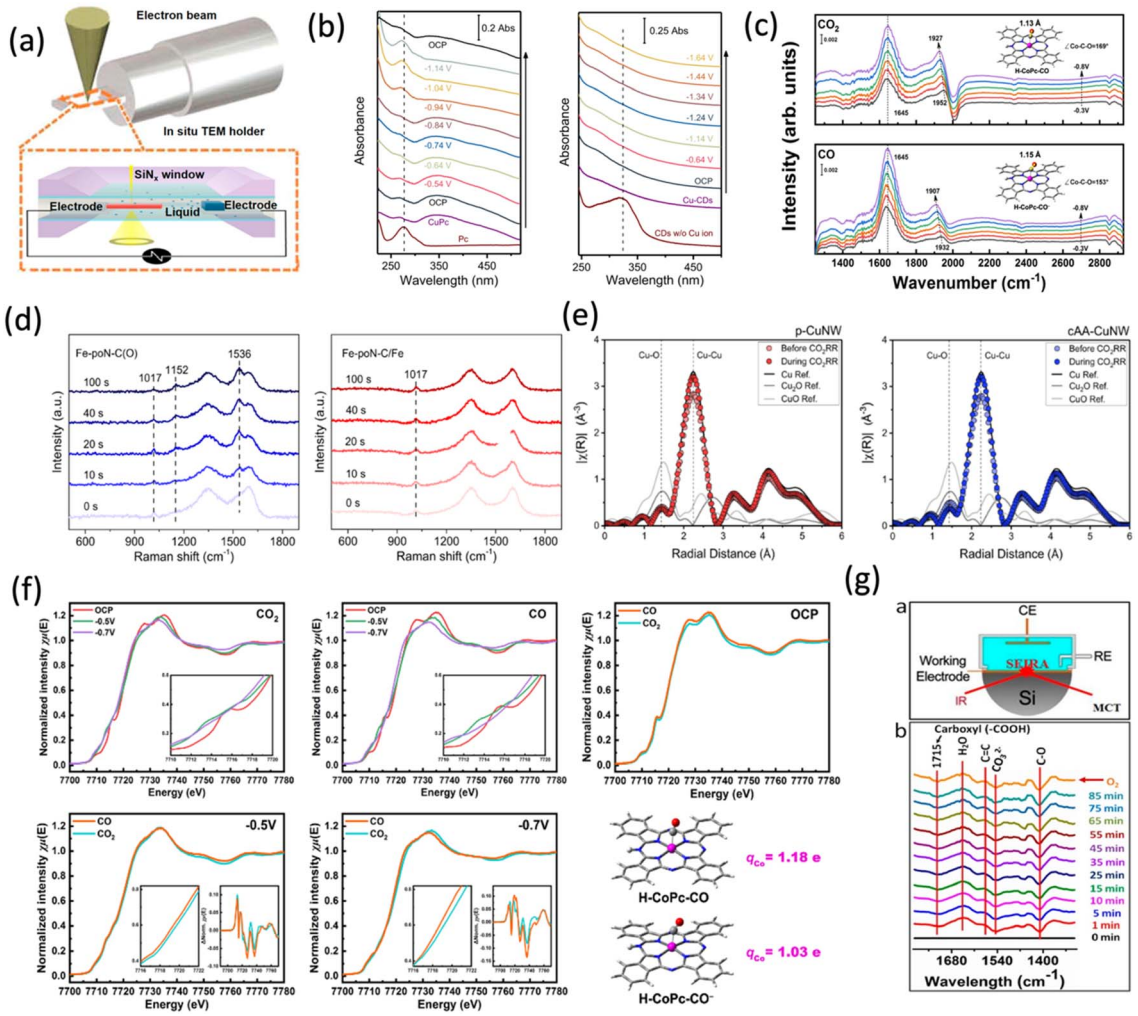

Fig. 7 *In situ* characterization (a) *In situ* TEM Configuration. Adapted with permission from ref. 74 Copyright 2020, American Chemical Society. (b) *In situ* UV-visible spectra of CuPc and Cu-CDs. Adapted with permission from ref. 75 Copyright 2021, Springer Nature. (c) *In situ* FTIR spectra of CoPc/MWCNT in CO_2−saturated (top) and CO-saturated (bottom) electrolytes, recorded at potentials of −0.3 V to −0.8 V *vs.* RHE. Adapted with permission from ref. 77 Copyright 2023 Springer Nature. (d) *In situ* Raman spectra of Fe-poN-C(O) and Fe-poN-C/Fe. Adapted with permission from ref. 76 Copyright 2023, Springer Nature (e) *operando* EXAFS spectra of *p*-CuNW and cAA-CuNW. Adapted with permission from ref. 78 Copyright 2024, Springer Nature. (f) Normalized Co K-edge XANES spectra for CoPc/MWCNT at open-circuit potential (OCP), $E = -0.5$ V, and $E = -0.7$ V *vs.* RHE in CO_2 and CO-saturated electrolytes. Adapted with permission from ref. 77 Copyright 2023, Springer Nature. (g) Schematic of the ATR-SEIRAS setup, and real-time ATR-SEIRAS spectra of GNDs-160 in a CO_2-saturated 0.5 M $KHCO_3$ solution at −0.68 V *vs.* RHE. Adapted with permission from ref. 79 Copyright 2021, Springer Nature.

© 2025 The Author(s). Published by the Royal Society of Chemistry

Open Access Article. Published on 07 maí 2025. Downloaded on 23.5.2026 05:53:41.
This article is licensed under a Creative Commons Attribution-NonCommercial 3.0 Unported Licence.

electrical, and thermal stimuli during TEM analysis (Fig. 7a).[74] *In situ* spectroscopic techniques, such as UV-vis, Raman, and FTIR can facilitate real-time monitoring of catalytic processes. UV-vis absorption spectroscopy is used to study catalytic reactions in both homogeneous and heterogeneous systems. Recently, Chai *et al.* utilized *in situ* UV-visible spectroscopy to reveal that copper-doped carbon dots (Cu-CDs) retain their single-site Cu configuration, confirming their intrinsic catalytic activity without forming metallic clusters. In contrast, Cu-phthalocyanine (CuPc) transforms into Cu clusters under electrochemical conditions (Fig. 7b).[75] Raman spectroscopy is widely used to analyze the evolution of catalyst surface adsorbates during ECR. As presented in Fig. 7d,[76] Raman spectroscopy revealed that the Fe–N_4 catalyst on an oxygenated carbon matrix forms $*CO_2^-$ intermediates during ECR, while the Fe–N–C catalyst with iron nanoparticles showed no $*CO_2^-$ peaks, suggesting rapid protonation to *COOH intermediates, indicating enhanced protonation on the iron surface. Compared to the above two methods, FTIR spectroscopy, with its high sensitivity and fast characterization speed, is especially effective for identifying reaction intermediates. It provides real-time, molecular-level insights into the adsorption and desorption of intermediates by analyzing the absorption of infrared light, offering insights into bond changes and molecular interactions, as shown in Fig. 7c.[77] *In situ* X-ray absorption spectroscopy (XAS) uses synchrotron radiation to probe the chemical and structural properties of catalysts with subatomic resolution. It is divided into XANES and EXAFS. EXAFS reveals changes in coordination environments (Fig. 7e),[78] while XANES helps determine the oxidation state (Fig. 7f).[77] Attenuated total reflectance–surface-enhanced infrared absorption spectroscopy (ATR-SEIRAS) can be used to study how the electric double layer (EDL) structure changes under the applied potential during electrocatalytic processes, including the reduction of CO_2. As shown in Fig. 7g,[79] ATR-SEIRAS at −0.68 V *vs.* RHE reveals stable carboxyl (−COOH) groups on metal-free single-layer graphene nanodisks (GNDs) during CO_2RR, with no significant change after oxygen saturation, indicating surface inertness.

5. Application of graphene-based catalysts for eCO_2RR

5.1 Metal-free heteroatom doped graphene for eCO_2RR

5.1.1 Single-heteroatom: N-doped graphene. N-doped graphene-based materials exhibit excellent catalytic performance for CO and formate production in terms of activity, selectivity, and stability, outperforming many noble metal catalysts. However, the precise nature of their active sites remains unclear due to the coexistence of multiple nitrogen species and the difficulty in correlating structural features with catalytic activity. Nonetheless, an increasing number of metal-free N-doped graphene-based materials have demonstrated significant potential as efficient catalysts for eCO_2RR.

Among all nitrogen configurations in N-doped graphene catalysts, pyridinic-N, characterized by a pair of lone electrons, exhibits a strong binding affinity for CO_2. This interaction facilitates the formation of the *COOH intermediate *via* proton-electron coupling, followed by its conversion to CO through *CO adsorption. In contrast, the electrons in graphitic-N occupy π–π antibonding orbitals, rendering them less favourable for CO_2 binding. As a result, the preferential adsorption of weakly acidic CO_2 molecules occurs more readily at pyridinic-N sites, promoting selective eCO_2RR on these sites rather than on graphitic-N.[8] Further studies showed that increasing the pyridinic-N concentration correlated with enhanced CO selectivity. Early reports on N-doped NCNTs enriched with pyridinic-N demonstrated a CO FE of ∼80% at a low overpotential of −0.18 V *vs.* RHE, highlighting the role of pyridinic-N as the active site for eCO_2RR.[80] N-doped CNTs with a high concentration of pyridinic-N sites (62.3% of all nitrogen) achieved a CO FE of 96% with a j_{CO} of 22 mA cm^{-2} at −0.7 V *vs.* RHE, emphasizing the dominant role of pyridinic-N in promoting eCO_2RR.[81] Subsequent work demonstrated that local curvature modulation of CNTs could further enhance the electronic environment of pyridinic-N, boosting CO selectivity to nearly 100%.[82]

Similarly, Wang *et al.*[83] designed hierarchically structured porous N-doped carbon membranes (Fig. 8a) combined with CNTs (HNCM/CNTs), achieving a formate FE of 81% at −0.9 V *vs.* the RHE in 0.1 M $KHCO_3$ solution (Fig. 8b and c). The catalyst demonstrated high selectivity for formate, along with excellent long-term stability of 36 hours and a significant current density. The study attributed the pyridinic N (41.8%) as the key active sites, playing a crucial role in CO_2 adsorption and activity enhancement.

In contrast, Zhang *et al.*[39] challenged conventional assumptions by demonstrating that graphitic-N, rather than pyridinic-N, promotes CO_2 reduction. Using template-assisted pyrolysis, they synthesized N-doped carbon foams (Fig. 8d) with tunable N species and achieved a CO FE of 95% at −0.5 V *vs.* RHE in 0.5 M $KHCO_3$ (Fig. 8e). DFT calculations revealed that the graphitic-N doped C atoms are more selective for CO_2 reduction to CO over HER, whereas pyridinic-N doped C atoms tend to favor HER over eCO_2RR, and pyrrolic-N doping reduces activity for both reactions (Fig. 8f). In addition, compared to metal catalysts, the sp^2 framework in the carbon matrix enhances the durability of heteroatom-doped graphene-based materials. The nitrogen active sites remain stable within the sp^2 carbon structure, resisting reconstruction and aggregation even at low doping levels.

Similarly, Li *et al.*[67] reported a 2D N-doped graphene-like carbon (Fig. 8g) achieving 95% FE for CO at −0.72 V *vs.* RHE (Fig. 8h), with j_{CO} of 9.07 mA cm^{-2}. They demonstrated that high-temperature pyrolysis increased defect density and porosity, enhancing the exposure of graphitic-N sites (Fig. 8i). DFT calculations indicated that C atoms adjacent to graphitic-N were the most catalytically active. Moreover, Zhou *et al.* and Liu *et al.* suggested that in certain nanostructured carbons (*e.g.*, CNTs or graphene nanoribbons), both pyridinic and graphitic-N may act as indistinguishable or co-active sites, complicating the mechanistic understanding.

While N-doped graphene-based materials have been extensively studied for the electrochemical reduction of CO_2 to C_1 products, recent advancements have demonstrated their

Open Access Article. Published on 07 mai 2025. Downloaded on 23.5.2026 05:53:41.
This article is licensed under a Creative Commons Attribution-NonCommercial 3.0 Unported Licence.

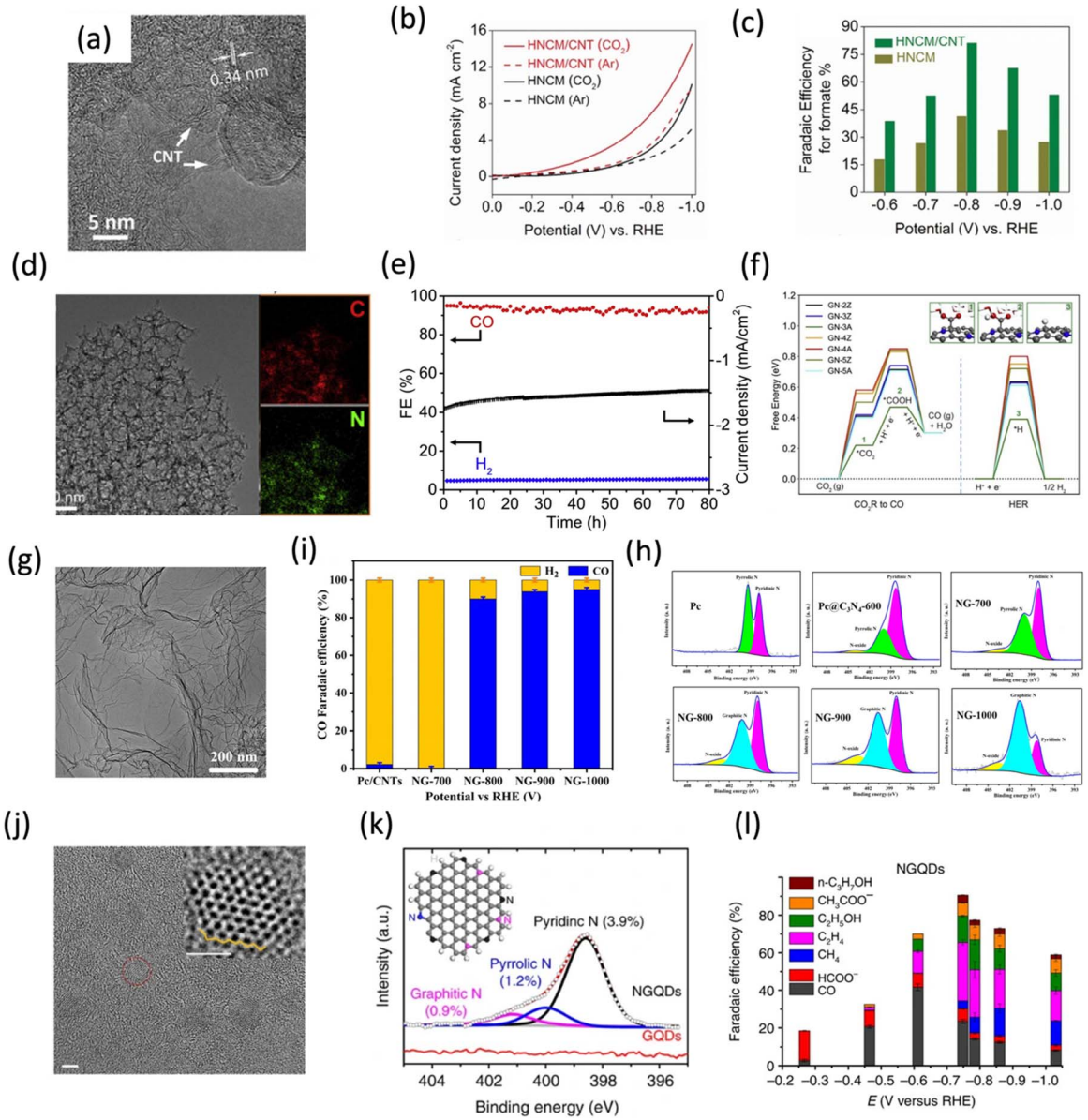

Fig. 8 N-doped graphene for eCO_2RR (a) HRTEM image of HNCM/CNT. (b) LSV curves recorded at a scan rate of 5 mV s^{-1} in CO_2-saturated and Ar-saturated 0.1 M $KHCO_3$ aqueous electrolyte. (c) FE for formate production as a function of applied potential at HNCM and HNCM/CNT electrodes. Adapted with permission from ref. 83 Copyright 2017, Wiley. (d) TEM image of NC-1100 and corresponding EDX maps of the NC-1100. (e) Stability test of the NC-1100 at 0.5 V *versus* RHE. (f) Free energy pathways for eCO_2RR to CO and HER over GN-induced active sites at 0 V *versus* RHE. Adapted with permission from ref. 39 Copyright 2020, Elsevier. (g) TEM images of NG-1000. (h) High-resolution XPS analysis in N1s region of *Pc* and various NG catalysts. (i) FE for CO at −0.72 V *vs.* RHE for different catalysts. Adapted with permission from ref. 67 Copyright 2021, Elsevier. (j) High-magnification TEM image of NGQDs. The inset shows a single NGQD containing zigzag edges, as circled. (k) High-resolution N1s spectrum for NGQDs. (l) FEs for NGQDs at various cathodic potentials. Adapted with permission from ref. 84 Copyright 2016, Springer Nature.

potential for producing economically valuable C_2 products, such as ethylene and ethanol. In this context, Wu *et al.*[84] reported the use of N-doped NGQDs (Fig. 8j and k) as effective catalysts for eCO_2RR. Operating within a flow cell electrolyzer using 1 M KOH as the electrolyte, NGQDs exhibited a total CO_2 reduction FE of up to 90% at −0.75 V *vs.* RHE. Notably, the catalyst favored C_2 product formation, achieving a combined FE of 45% for ethylene and ethanol, with partial current densities of 46 mA cm^{-2} and 21 mA cm^{-2} for C_2H_4 and C_2H_5OH, respectively (Fig. 8l). Although NGQDs demonstrate the potential for selective C_2 product formation, the FE for individual products remains relatively low compared to state-of-the-art Cu-based catalysts, which are currently the benchmark for multi-carbon product generation. To address this limitation, strategies such as increasing N dopant density or co-doping with complementary heteroatoms (*e.g.*, B, S, P) may enhance both the activity and selectivity toward specific C_2 products. Furthermore, the C–C bond formation mechanism over N-doped

© 2025 The Author(s). Published by the Royal Society of Chemistry

Open Access Article. Published on 07 mai 2025. Downloaded on 23.5.2026 05:53:41.
This article is licensed under a Creative Commons Attribution-NonCommercial 3.0 Unported Licence.

carbon catalysts remains poorly understood, posing a significant challenge for the development of next-generation metal-free graphene-based electrocatalysts tailored for efficient and selective multi-carbon product synthesis.

5.1.2 Other single-heteroatom doped graphene. Beyond nitrogen doping, other single-heteroatom dopants such as boron and phosphorus have shown promising potential in enhancing the electrocatalytic performance of graphene-based materials for CO_2 reduction. Boron-doped graphene (BG) has been shown to promote CO_2 chemisorption by altering the surface electronic structure, thereby enabling its catalytic activity toward formate production *via* eCO_2RR.[40] Phani *et al.*[85] were the first to report on the electrocatalytic performance of BG, demonstrating that catalysts synthesized by heating GO and boric acid at 900 °C in a CO_2 atmosphere achieved a formate FE of 66% at −1.4 V *vs.* SCE, outperforming the benchmark Bi catalyst (Fig. 9a). XPS signals of B1s and C1s confirmed the incorporation of boron atoms within the hexagonal graphitic structure (Fig. 9b and c), and computational studies combined with experimental results revealed that boron doping induces an uneven distribution of spin density in graphene, enhancing its catalytic activity for CO_2 adsorption and reduction compared to pristine graphene. DFT calculations confirmed the feasibility of CO_2 physisorption and chemisorption on BG, leading to formate. Similarly, boron-doped diamond has exhibited excellent activity for formate production, achieving a high FE of 94.7% at a current density of 2 mA cm^{-2} in 0.5 M KCl, with stable operation for 24 hours in a flow-cell system.[86] These findings emphasize BG's potential as a cost-effective alternative to metal-based electrocatalysts for carbon dioxide utilization.

Phosphorus doping in graphene significantly modifies its electronic structure and active site distribution, enabling enhanced catalytic activity for ECR to C_2 products. Unlike N-doping, where the adjacent carbon atoms often serve as the active sites due to electronic redistribution, P atoms themselves act as positively charged active sites due to the reversed polarity of the C–P bond, stemming from phosphorus's lower electronegativity (2.19) compared to carbon (2.55).[87] Additionally, the larger atomic radius of P introduces lattice distortion and abundant edge defects, which are beneficial for C–C coupling. Motivated by these properties, Yang *et al.*[19] synthesized phosphorus-doped graphene aerogels (PGAs) *via* hydrothermal reduction of GO with phosphoric acid (Fig. 9d). Using an H-type three-electrode cell with CO_2-saturated 0.5 M $KHCO_3$ electrolyte, PGA-2 achieved a FE of 48.7% for ethanol production at −0.8 V *versus* RHE, with an ethanol yield of 14.62 μmol $h^{-1}cm^{-2}$ and stability maintained for 70 hours (Fig. 9e and f). It was revealed that the catalyst's hierarchical porous structure enhanced CO_2 adsorption and charge transfer, while DFT calculations showed that P-doping at graphene zigzag edges promoted *CO dimerization and C–C coupling. This work inspires the design of metal-free catalysts by using P-doped graphene-based materials for the conversion of CO_2 into high-value C_2 products with high efficiency, selectivity, and stability.

5.1.3 Co-heteroatom doped graphene. Although single heteroatom doped graphene-based materials have been shown to serve as efficient, metal-free alternatives to traditional metal-based electrocatalysts for CO_2 reduction, co-doping with a second heteroatom such as boron, sulphur, or phosphorus has been demonstrated to further enhance their electronic properties and surface polarity, significantly improving their performance. Specifically, incorporating S into N-doped graphene was proposed to enhance the asymmetrical spin density of the carbon system due to the higher polarizability of S atoms

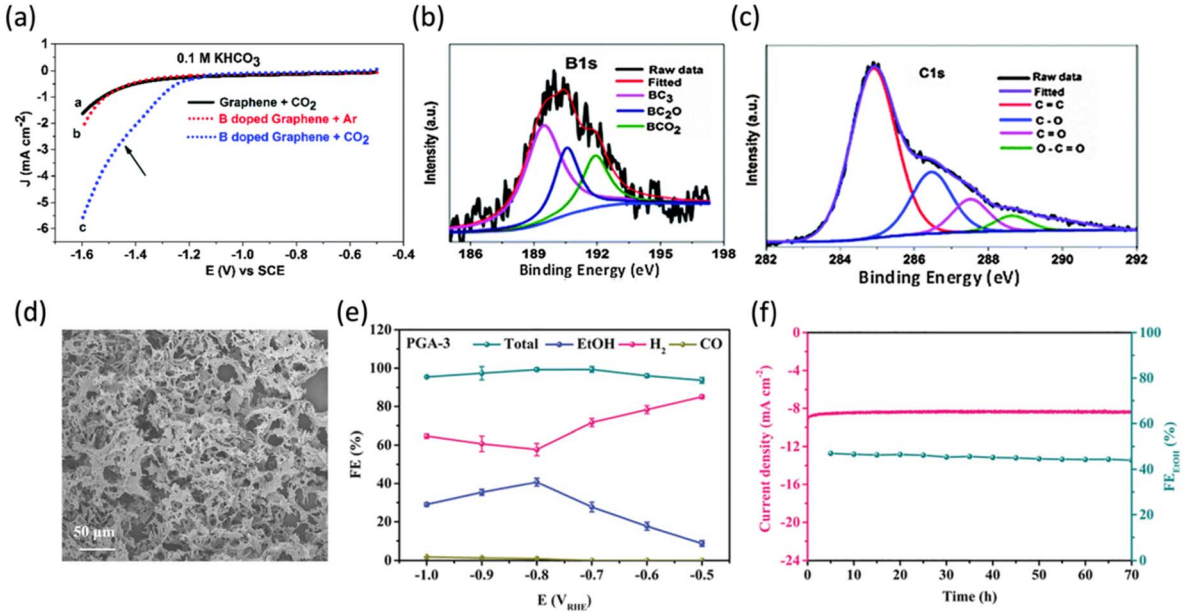

Fig. 9 Other heteroatom doped graphene for eCO_2RR High-resolution XPS spectra of (a) B1s and (b) C1s (c) LSV of BG and Bi in 0.1 M $KHCO_3$ in the presence of CO_2. Adapted with permission from ref. 85 Copyright 2015, Royal Society of Chemistry. (d) SEM image of PGA-2. (e) Stability test on PGA-2. (f) FE for EtOH and yield for PGA-2 in a flow cell. Adapted with permission from ref. 19 Copyright 2022, Wiley.

Open Access Article. Published on 07 mai 2025. Downloaded on 23.5.2026 05:53:41.
This article is licensed under a Creative Commons Attribution-NonCommercial 3.0 Unported Licence.

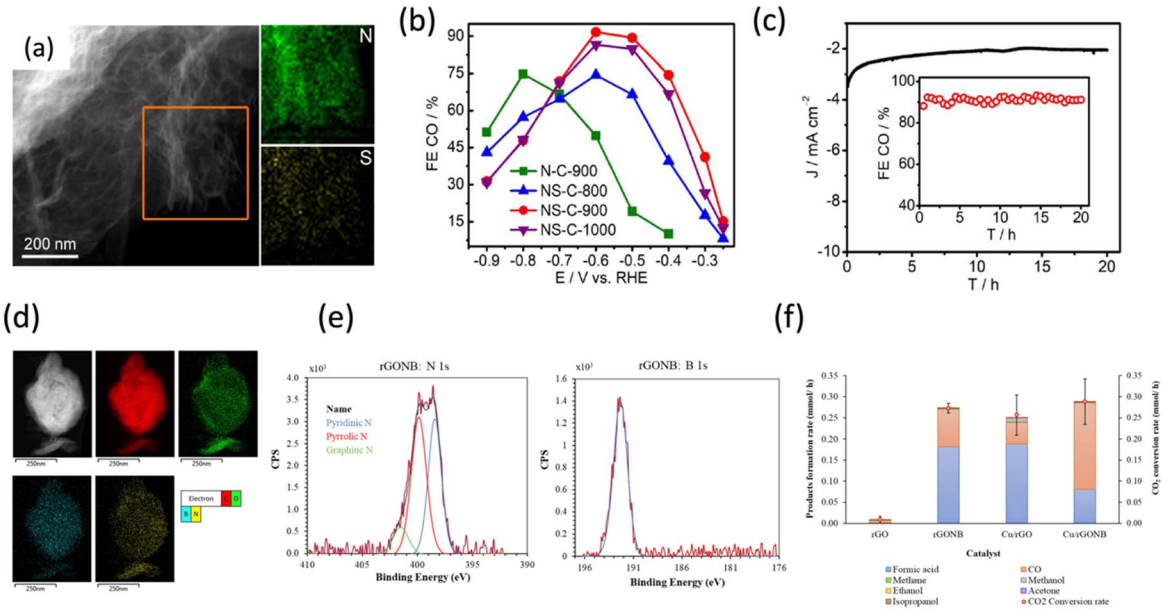

Fig. 10 Co-heteroatom doped graphene for eCO_2RR (a) scanning TEM and N,S elemental mapping images of NS-C-900. (b) FE for CO *vs.* applied potential. (c) Chronoamperometric responses and CO FEs at −0.6 V on NS-C-900 for stability tests. Adapted with permission from ref. 61 Copyright 2019, Elsevier. (d) Elemental mapping of rGONB (using STEM-HAADF). (e) XPS spectra of N1s spectrum and B1s spectrum. (f) FE for CO_2 reduction products and CO_2 conversion rate with rGO and rGONB catalysts *vs.* Cu-based catalysts (Cu/rGO and Cu/rGONB) under experimental conditions. Adapted with permission from ref. 91 Copyright 2023, Elsevier.

compared to N and C, which is beneficial for CO_2 activation and the binding of intermediates of eCO_2RR.[88–90] Thus, considering the synergistic effect between N and S, Pan *et al.*[61] developed N–S Co-doped configurations *via* a pyrolysis strategy (Fig. 10a) and demonstrated that sulfur addition to N-doped carbon significantly enhances the electrochemical reduction of CO_2 to CO. The N, S co-doped carbon (NS–C) catalyst exhibited a maximum CO FE of 92% and a CO current density of 2.63 mA cm^{-2} at a low overpotential of 490 mV, outperforming the S-free N–C catalysts (Fig. 10b and c). Sulfur incorporation facilitated the formation of pyridinic nitrogen as active CO_2 reduction sites and decreased the free energy barrier for the *COOH intermediate formation, synergistically enhancing catalytic activity and selectivity.

In addition, Cerrillo *et al.*[91] demonstrated that nitrogen and boron co-doped reduced graphene oxide (rGONB) (Fig. 10d) effectively catalyzes the electrochemical reduction of CO_2 in a PEM-type cell operating in gas-phase and continuous mode, and the XPS signals of N1s and B1s indicate the incorporation of boron atoms into the hexagonal graphene lattice (Fig. 10e). The catalyst achieved a CO_2 conversion rate 30 times higher than undoped rGO (Fig. 10f), with formic acid and CO as the primary products. The electron-donating nitrogen species and electron-accepting oxidized boron sites synergistically enhanced catalytic activity, outperforming Cu/rGO in CO_2 conversion efficiency.

5.2 Graphene-metal hybrid catalysts

5.2.1. Single-atom catalysts on graphene. SACs are catalysts in which isolated metal atoms are individually dispersed on a support, offering maximum atom utilization and uniform active sites. The support material plays a critical role in stabilizing isolated metal atoms, which, due to their high surface energy, require strong bonding to prevent aggregation. Common stabilization strategies include anchoring single atoms onto oxide supports such as FeO_x,[92] CeO_2,[93] or Al_2O_3,[94] or incorporating them into single-atom alloys (SAAs).[95] However, these approaches still face significant challenges, such as sintering under reducing conditions, complex synthesis procedures, and limited metal loading capacity.[96] In contrast, graphene-based supports, including N-doped graphene-based materials or mesoporous graphitic carbon nitride ($g\text{-}C_3N_4$) offer robust metal coordination environments.

Over the past decade, SACs supported on such graphene-based materials have garnered significant attention due to the synergistic benefits of atomically dispersed active sites and highly conductive and chemically tunable graphene-based frameworks.[97] A notable advancement in this area is the development of M–N–C SACs (M = Fe, Co, Ni, Cu), where metal atoms are stabilized in well-defined $M\text{–}N_x$ coordination environments. These materials feature well-defined coordination environments and exhibit excellent performance in electrocatalysis. For example, $M\text{–}N_4$ sites on graphene support have demonstrated exceptional activity and selectivity for electrochemical CO_2 reduction to CO, achieving FE > 90%.[98] Despite the high per-atom activity of these catalysts, maintaining high metal loadings without aggregation remains a key challenge, driving continued research in synthesis strategies to enhance both stability and performance.

Beyond isolated $M\text{–}N_4$ sites, emerging strategies to tailor the coordination environment of SACs have unlocked new pathways to enhance both activity and operational stability. Notably,

© 2025 The Author(s). Published by the Royal Society of Chemistry

Open Access Article. Published on 07 maí 2025. Downloaded on 23.5.2026 05:53:41.
This article is licensed under a Creative Commons Attribution-NonCommercial 3.0 Unported Licence.

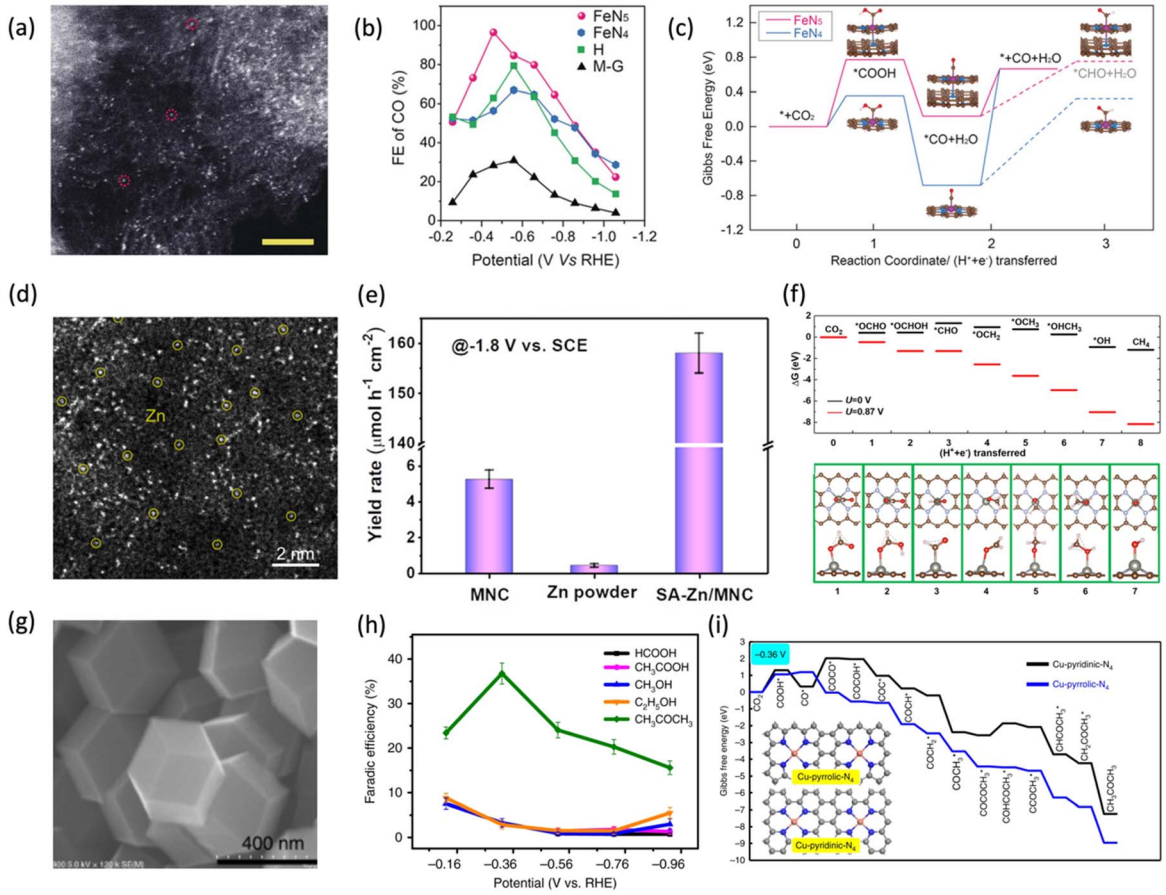

Fig. 11 Single-atom catalysts on graphene for eCO_2RR (a) magnified STEM images of uniformly distributed single Fe atoms in graphene (single Fe atoms are highlighted with dashed circles). (b) FE for CO *vs.* applied potential. (c) Free-energy profile with optimized intermediates for electroreduction of CO_2 to CO, determined using the computational hydrogen electrode (CHE) model. Adapted with permission from ref. 100 Copyright 2019, Wiley. (d) Atomic-resolution HAADF-STEM image (Zn atoms are highlighted with yellow circles). (e) FE for methane *vs.* applied potential. (f) Free energy diagrams for ERC to CH_4 on Zn–N_4–graphene, showing the most stable structure of each step. Red and pink balls represent O and H atoms, respectively. Adapted with permission from ref. 103 Copyright 2020, American Chemical Society. (g) SEM images of Cu-SA/NPC. (h) FE for CO_2 reduction products for Cu-SA/NPC. (i) Free energy diagrams calculated at a potential of −0.36 V for CO_2 reduction to CH_3COCH_3 on Cu-pyridinic-N_4 and Cu-pyrrolic-N_4 sites of Cu-SA/NPC. Adapted with permission from ref. 104 Copyright 2020, Springer Nature.

recent advances demonstrate that certain M–N_x configurations can simultaneously achieve exceptional catalytic efficiency and durability.[99] For instance, Zhang *et al.*[100] demonstrated that single-atom Fe–N_5 sites, formed when an axial ligand coordinates with Fe–N_4 during prolonged thermal pyrolysis of N-doped graphene(Fig. 11a), exhibit exceptional catalytic activity and durability for the electrochemical CO_2 reduction to CO in aqueous media, outperforming the Fe–N_4. The FeN_5 catalyst achieved a FE of 97.0% at a low overpotential of 0.35 V and demonstrated excellent durability with less than 2% current decay and stable CO selectivity (~97%) over 24 h at −0.46 V *vs.* RHE, while preserving the atomic FeN_5 configuration post-reaction (Fig. 11b). DFT calculations revealed that the additional axial pyrrolic nitrogen ligand in the FeN_5 site causes an additional reduction in electron density of Fe 3d orbitals, which weakens the bonding interaction with CO and enables the rapid desorption of CO along with high selectivity for CO production (Fig. 11c).

Although most SAs coordinated on graphene-based materials primarily produce CO as the main product,[56] some catalysts have also been reported to generate hydrocarbons.[101,102] The single-atom Zn catalysts supported on N-doped carbon (SA-Zn/MNC) (Fig. 11d) reported by Han *et al.*[103] selectively reduce CO_2 to methane, achieving a FE of 85% for CH_4 production at −1.8 V *vs.* SCE (Fig. 11e) with a partial current density of −31.8 mA cm^{-2} and stability over 35 hours without significant performance degradation. The stable and efficient performance of the catalyst can be attributed to the graphene's high electrical conductivity, which ensures rapid charge transport. Theoretical calculations revealed that during ECR, the O atom in the *OCHO intermediate preferentially bonds with Zn instead of the C atom, thereby suppressing CO formation and favoring CH_4 production (Fig. 11f).

While SACs have demonstrated excellent performance for eCO_2RR to C_1 products, the formation of multi-carbon products remains a significant challenge due to the absence of adjacent

Open Access Article. Published on 07 mai 2025. Downloaded on 23.5.2026 05:53:41.
This article is licensed under a Creative Commons Attribution-NonCommercial 3.0 Unported Licence.

active sites typically required for C–C coupling. The incorporation of atomically dispersed Cu into nitrogen-doped graphene frameworks has emerged as a compelling strategy to address this limitation by enabling unconventional C–C coupling pathways within a single-atom coordination environment. Graphene provides a highly conductive, chemically tunable support, while nitrogen doping, particularly pyrrolic-N, strongly coordinates single Cu atoms and alters their electronic structure. This coordination environment allows two CO* intermediates to adsorb sequentially on the same Cu site, where intramolecular coupling occurs at a single metal center, leading to C–C bond formation. Zhao *et al.*[104] demonstrated that Cu atoms anchored on nitrogen-doped porous carbon (Cu-SA/NPC) exhibited (Fig. 11g) a FE of 36.7% (Fig. 11h) for acetone production, with a notable rate of 336.1 μg h^{-1} at low overpotential. DFT studies revealed that the pyrrolic-N coordinated Cu sites lower the energy barriers for both CO_2 activation and CO–CO coupling, enabling the formation of key intermediates for C_3 product generation (Fig. 11i). This work highlights the ability of graphene-based SACs to host complex reaction pathways, offering new insights for the rational design of efficient and selective metal-free or atom-efficient CO_2RR systems targeting C_{2+} products. The co-doping of multiple species of foreign atoms may generate new properties or create synergistic effects.

5.2.2. Dual-atom catalysts on graphene. While SACs have demonstrated significant promise in eCO_2RR due to their high atomic efficiency and well-defined active sites, their limitations, including a fixed adsorption mode determined by a single active site and the inability to independently optimize adsorption energies for different intermediates due to linear scaling relationships, have prompted interest in DACs. In contrast, DACs feature two adjacent metal centres, offering unique opportunities to tune electronic structures, break linear scaling relationships, and facilitate CO_2 adsorption in bent configurations, thereby enhancing CO_2 activation efficiency.

Li *et al.*[105] reported a highly active N-coordinated DAC by embedding Ni–Fe sites within ZIF-derived porous carbon (Fig. 12a), aiming to overcome the limitations of traditional M–N–C SACs in eCO_2RR. Among the structures studied, the 2N-bridged (Fe–Ni)N_6 configuration featuring FeN_4 and NiN_4 sites linked by two shared nitrogen (Fig. 12b) atoms showed the most promising performance. This dual-metal synergy facilitated optimal *COOH adsorption and *CO desorption, addressing

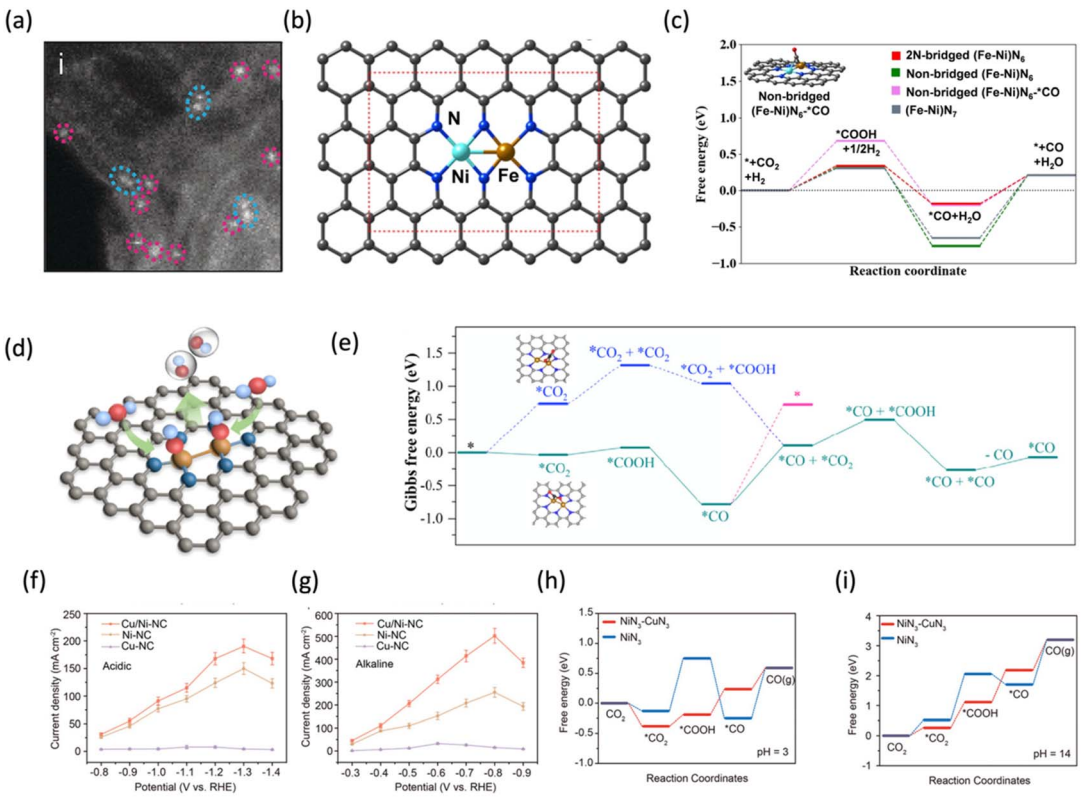

Fig. 12 Dual-atom catalysts on Graphene for eCO_2RR (a) HAADF-STEM images illustrating metal atom dispersion on a carbon support: formation of atom pairs/clusters (cyan) *versus* isolated single atoms (magenta). (b) Structural model of N-coordinated dual-metal Ni–Fe sites. (c) Calculated free energy diagram for electrochemical CO_2 reduction (eCO_2RR) on various dual-metal Fe–Ni sites. Adapted with permission from ref. 105 and 128 Copyright 2022, Wiley. (d) Structural model of Fe_2NPC dual-atom catalysts (DACs). (e) Gibbs free energy profile for electrochemical CO_2 reduction on Fe_2NPC. Adapted with permission from ref. 110 and 128 Copyright 2022, American Chemical Society. (f) Corresponding partial current density for CO at different applied potentials in acidic electrolyte. (g) Partial current density for CO in alkaline electrolyte. (h) Gibbs free energy diagram for CO_2-to-CO conversion over NiN_3–CuN_3 and NiN_3 with pH correction at pH = 3. (i) Gibbs free energy diagram at pH = 14. Adapted with permission from ref. 112 Copyright 2023, Wiley.

© 2025 The Author(s). Published by the Royal Society of Chemistry

Open Access Article. Published on 07 mai 2025. Downloaded on 23.5.2026 05:53:41.
This article is licensed under a Creative Commons Attribution-NonCommercial 3.0 Unported Licence.

the strong CO* binding that lowers the reactivity of FeN_4,[106] and the weak *COOH binding of NiN_x sites.[107,108] DFT calculations revealed favourable charge redistribution between the Ni and Fe centres, reducing the energy barrier for *CO desorption and enhancing the onset potential for CO_2RR, while suppressing HER activity (Fig. 12c). Beyond experimental advances, theoretical studies also have played a key role in guiding DACs design. For instance, Luo *et al.* used DFT calculations to investigate dual-metal site catalysts like Cu/Mn, Ni/Mn, and Ni/Fe, which showed enhanced activity for CO_2-to-CO conversion due to the breaking of the conventional scaling relationship between *CO and *COOH adsorption, allowing more favourable reaction pathways.[109]

Similarly, Zhao *et al.*[110] prepared a homonuclear Fe–Fe DAC featuring Fe_2N_6 sites uniformly anchored on nitrogen-doped porous carbon (Fig. 12d). This Fe–Fe DAC reached a FE of 96.0% for CO production at −0.6 V *vs.* RHE with a low Tafel slope of 60 mVdec^{-1}, markedly outperforming Fe SACs. DFT studies reveal that the cooperative interaction between the two Fe centres facilitates the adsorption of CO_2 in a bent configuration, effectively reducing the activation barrier and promoting rapid *CO desorption (Fig. 12e). Similarly, Hao and co-workers found that Ni/Ni DMSCs could also achieve over 99% FE for CO production, indicating that even homonuclear DACs can achieve exceptional eCO_2RR performance when properly configured.[111]

Demonstrating the potential of advanced dual-atom catalyst systems, Zhang *et al.*[112] developed a Ni–Cu DAC embedded in hollow N-doped carbon nanocages that exhibited pH-universal activity for CO_2 reduction. The catalyst demonstrated near-unity CO FE up to 99% across acidic, neutral, and alkaline electrolytes (Fig. 12f and g), with high partial current densities (up to 489 mA cm^{-2} in alkaline). Under acidic conditions, where HER typically dominates, the catalyst retained a CO selectivity of 98.5% and achieved a remarkable CO_2 utilization efficiency of 64.3%. *Operando* characterizations and DFT analysis revealed that Cu shifted the Ni d-band center closer to the Fermi level,

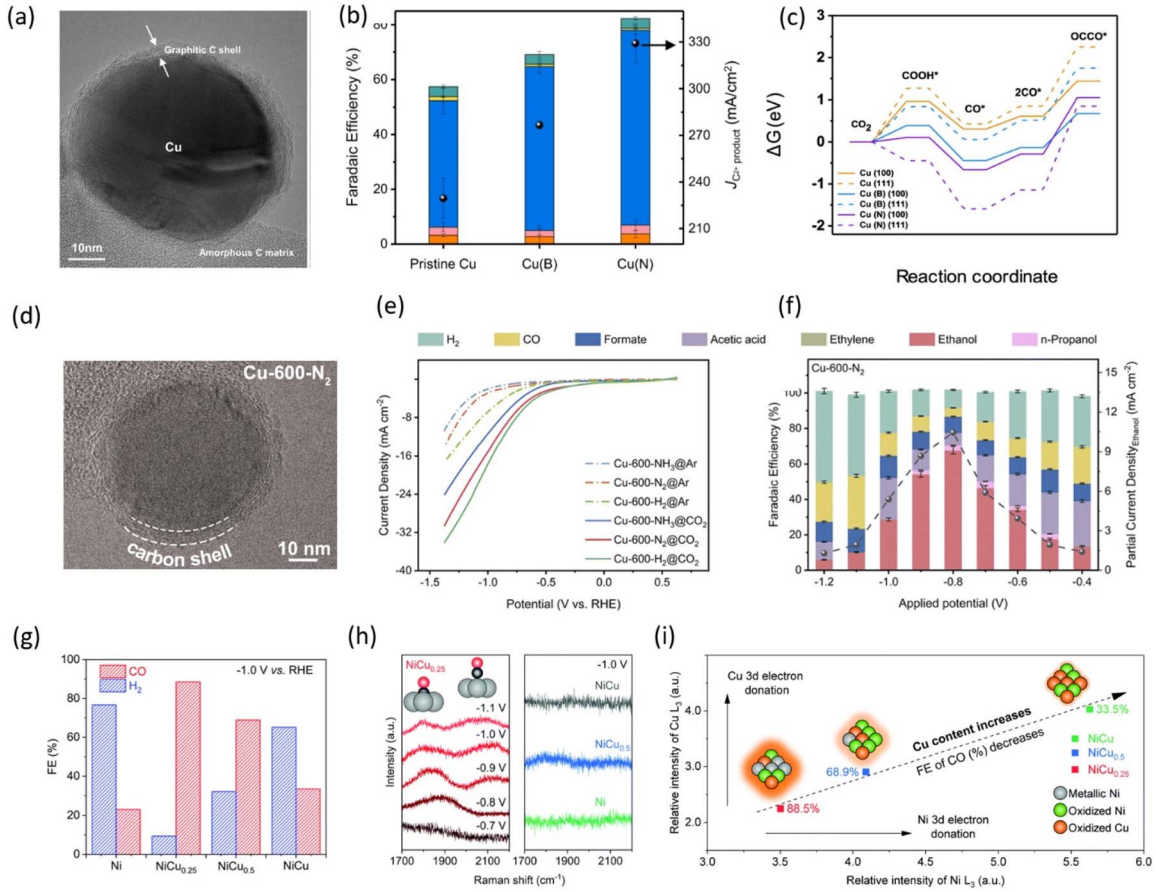

Fig. 13 Graphene-shell encapsulated metal nanoparticles for eCO_2RR (a) high-resolution TEM image of the confined Cu nanoparticles and quasi-graphitic C shell. (b) FE and partial current density for C_{2+} products at 400 mA cm^{-2}. (c) Free energy diagram for CO dimerization on the pristine Cu, Cu (B), and Cu (N) surfaces. Adapted with permission from ref. 68 Copyright 2021, Springer Nature. (d) TEM images of Cu-600-N_2. (e) LSV curves in CO_2 and Ar-saturated 0.1 M $KHCO_3$ aqueous solutions for Cu-600-N_2, Cu-600-H_2, and Cu-600-NH_3. (f) FE and partial current density for Cu-600-N_2. Adapted with permission from ref. 127 Copyright 2023, Royal Society of Chemistry. (g) FE distributions at 1.0 V *vs.* RHE. (h) *In situ* Raman spectroscopy results. Left: Potential-dependent Raman spectra of $NiCu_{0.25}$, with adsorption models illustrating *CO adsorption at bridge and atop sites on the catalyst surface. Right: Raman spectra of other catalysts recorded at an applied potential of 1.0 V *vs.* RHE. (i) Electron donation and CO selectivity trend with increasing Cu content in $NiCu_x$. Glow intensity represents 3d electron density in molecular models. Adapted with permission from ref. 128 Copyright 2017, Royal Society of Chemistry.

Open Access Article. Published on 07 mai 2025. Downloaded on 23.5.2026 05:53:41.
This article is licensed under a Creative Commons Attribution-NonCommercial 3.0 Unported Licence.

thus enhancing *COOH formation and tuning the binding energies of key intermediates (Fig. 12h and i).

5.2.3. Graphene-shell-encapsulated nanoparticles. Over the past decade, nanoparticles encapsulated in graphene-based materials have demonstrated great potential as electrocatalysts for electrochemical energy applications.[113–115] Graphene acts as a protective layer for catalysts in eCO_2RR by providing a chemically inert barrier that prevents catalyst reconstruction, particle aggregation, and oxidation.[116] Additionally, its high conductivity facilitates efficient electron transfer, ensuring sustained catalytic activity.[117]

Copper is widely studied for its ability to yield C_{2+} products such as ethylene, ethanol, and n-propanol with high selectivity. However, its structural instability under electrochemical reduction conditions is a major challenge, leading to catalyst reconstruction and reduced performance.[118–123] Degradation prevention methods, such as the use of physical barriers[124] on the surface and alloying with second metals,[125,126] have been proposed as solutions to mitigate this issue. Among these, the physical barrier method has been the most studied, with graphene emerging as the most suitable option due to its inert nature. Kim *et al.*[68] developed a catalyst system resistant to reconstruction by spontaneously depositing graphitic carbon, which surrounds the Cu nanoparticles in a quasi-graphitic C shell, thereby protecting them (Fig. 13a). This catalyst not only prevents Cu from reconstruction but also enables inner Cu doping to enhance activity and stability. Their copper nanoparticles encapsulated in quasi-graphitic carbon shells effectively catalyze the electrochemical conversion of CO_2 to C_{2+} products with no reconstruction. Using a flow-cell reactor with a 1 M KOH electrolyte, boron-doped Cu catalysts achieved a FE of 68.1% for ethylene production at −0.55 V *versus* RHE, while nitrogen-doped Cu catalysts attained an FE of 82.3% for C_{2+} products with a partial current density of 329 mA cm^{-2} (Fig. 13b). The quasi-graphitic carbon shell stabilized the Cu nanoparticles against reconstruction and enhanced C–C coupling, as confirmed by DFT calculations (Fig. 13c).

Similarly, Yao *et al.*[127] revealed that copper nanoparticles encapsulated in a carbon shell (Cu-600-N_2), synthesized by calcination of a copper-based metal–organic framework (Cu-MOF) in an N_2 atmosphere (Fig. 13d), effectively catalyze the electrochemical reduction of CO_2 to ethanol with high selectivity and stability. These Cu-MOFs were also exposed to various gas atmospheres, including H_2 and NH_3, to investigate their influence on the catalytic performance. The catalyst under N_2 achieved a FE of 67.8% at −0.8 V *vs.* RHE, outperforming copper nanoparticles synthesized under H_2 and NH_3 atmospheres (Fig. 13e and f). The carbon shell provided structural protection, preventing Cu particle aggregation and surface reconstruction, significantly enhancing catalyst stability over 16 hours of continuous operation. Additionally, Tafel analysis revealed superior corrosion resistance for Cu-600-N_2, attributed to its more positive corrosion potential than the other catalysts. This protective carbon layer and synergistic Cu–C interactions maintained high FE and current density, making Cu-600-N_2 a promising electrocatalyst for ethanol production in CO_2RR applications.

Moreover, Xu *et al.*[128] demonstrated that graphene-encapsulated nickel-copper bimetallic nanoparticles ($NiCu_{0.25}$) effectively catalyze the electrochemical reduction of CO_2 to CO. Using a CO_2-saturated 0.1 M $KHCO_3$ electrolyte, $NiCu_{0.25}$ achieved a FE of 88.5% at −1.0 V *versus* RHE (Fig. 13g), with enhanced stability due to the graphene encapsulation preventing particle aggregation. The study revealed that lower Cu content in $NiCu_x$ alloys optimizes the electronic structure, enhancing *COOH adsorption and CO selectivity. The graphene shell stabilizes the nanoparticles, preserving structural integrity. Fig. 13h confirms *CO adsorption variations, while Fig. 13i shows that increasing Cu content shifts electron donation, reducing CO selectivity. These results demonstrate the dual role of graphene as both a physical barrier and an electronic modulator, pointing to the potential of graphene-based encapsulation strategies in designing next-generation stable and selective CO_2 reduction catalysts.

5.2.4. Graphene-metal composite structures. Graphene, a two-dimensional material characterized by its high specific surface area and excellent electrical conductivity, serves as an ideal substrate for anchoring metal nanoparticles and clusters. The synergistic interactions between graphene and metal species promote efficient charge transfer, stabilize catalytically active sites, and modulate the local electronic structure enhancing electrocatalytic performance. For example, Yuan *et al.*[129] synthesized cu nanoparticles anchored on pyridoxine-functionalized graphene oxide (GO-VB_6-Cu) (Fig. 14a) to demonstrate efficient electrocatalytic performance for the electrochemical reduction of CO_2 to ethanol in an aqueous medium. The GO-VB_6-Cu catalyst achieved a FE of 56.3% at −0.25V *vs.* RHE with high stability, maintaining performance for over 24 hours (Fig. 14b). Electrochemical kinetic studies revealed that the enhanced catalytic performance of GO-VB6-Cu was primarily associated with significantly improved electron transfer at the electrode surface. This improvement was attributed to a combination of factors, including a large electrochemically active surface area (ECSA), enhanced CO_2 adsorption capacity, and reduced charge transfer resistance (Fig. 14c). Thus, the synergistic interaction between Cu nanoparticles and pyridoxine-functionalized graphene oxide enables efficient and selective electrochemical CO_2 reduction to ethanol at low overpotentials, effectively overcoming the high energy barriers typically associated with Cu surfaces. Similarly, Cu nanoparticles stabilized by reduced graphene oxide have shown enhanced ethanol selectivity and stability due to improved charge transfer and CO intermediate stabilization.[130] This further supports the role of graphene-based supports in modulating local electronic environments and catalytic pathways. These findings provide valuable insights for designing advanced metal graphene composites aimed at enhancing charge transfer and reducing overpotentials in CO_2 reduction reactions.

Moreover, despite the ability of copper-based electrocatalysts to convert CO_2 into value-added multicarbon products, the traditional Cu forms, such as foils or large nanoparticles, often suffer from limited active surface area utilization,[131,132] necessitating the development of nanoscale catalysts to optimize

© 2025 The Author(s). Published by the Royal Society of Chemistry

Open Access Article. Published on 07 mai 2025. Downloaded on 23.5.2026 05:53:41.
This article is licensed under a Creative Commons Attribution-NonCommercial 3.0 Unported Licence.

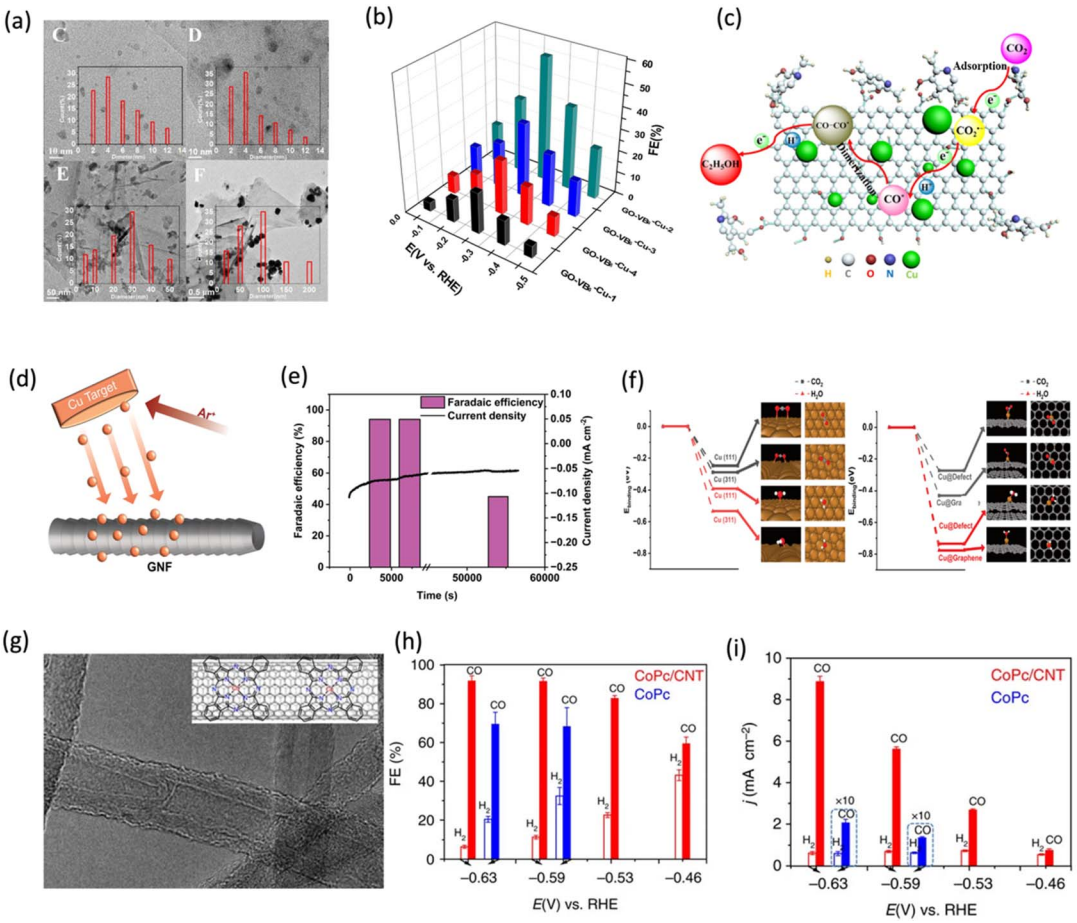

Fig. 14 Graphene-metal composite structures for eCO_2RR (a) TEM images of GO-VB6-Cu-*x*. (b) FEs for CO_2 reduction *vs.* applied potential for various GO-VB6-Cu catalysts. (c) Schematic illustration of the CO_2 electrochemical reduction process on the GO-VB6-Cu catalyst. Adapted with permission from ref. 129 Copyright 2019, Elsevier. (d) Schematic of magnetron sputtering delivering atoms of Cu directly onto the GNF surface. (e) FE and the current density for Cu/GNF (0.84 wt% Cu) at −0.38 V *vs.* RHE over time. (f) Binding energy of CO_2 and H_2O to Cu (111) and Cu (311) surfaces of bulk metal, Cu atom embedded in graphene vacancy defects, and pristine graphene. Adapted with permission from ref. 133 Copyright 2024, Nature. (g) TEM image of the CoPc/CNT (6%) hybrid with the chemical representation of the CoPc/CNT hybrid interface. (h) FE for CO and H_2 at various applied potentials for CoPc and CoPc/CNT electrodes. (i) Corresponding partial current densities for CO and H_2 for CoPc and CoPc/CNT under the same conditions. Adapted with permission from ref. 134 Copyright 2024, Nature.

performance. Cu nanoclusters, composed of a group of atoms, have been recognized as a solution in this context. However, the effectiveness of these catalysts is greatly influenced by the properties of the support material and the particular conditions during catalyst synthesis. In this regard, Burwell *et al.*[133] demonstrated that copper nanoparticles directly anchored onto graphitized carbon nanofibers (Cu/GNF) prepared *via* solvent-free atomic deposition (Fig. 14d) enhance the electrochemical reduction of CO_2 with remarkable selectivity. The Cu/GNF catalyst achieved a FE of 94% for formate production at −0.38 V *vs.* RHE (Fig. 14e), outperforming conventional Cu-based catalysts. The Cu nanoparticles (2–5 nm) localized at graphitic step edges provided a strong metal-support interface, facilitating charge transfer and stabilizing catalytic sites (Fig. 14f). The study highlighted the critical role of the graphitic step edges in stabilizing the Cu nanoparticles, which prevented aggregation and ensured efficient CO_2 conversion. These findings highlight the significance of designing well-defined nanoscale metal–graphene interfaces, which can effectively stabilize metal active sites, inhibit particle aggregation, and enhance both the activity and durability of CO_2 reduction catalysts.

In addition, immobilizing M–N–C-type molecular catalysts such as metal phthalocyanine or metal porphyrins onto conductive graphene-based materials has emerged as an effective strategy to improve both catalytic activity and stability for eCO_2RR. These graphene-based supports not only prevent catalyst aggregation and facilitate charge transport but also provide favorable electronic interactions that can modulate the local coordination environment of the metal center. For instance, Zhang *et al.*[134] reported that molecularly dispersed CoPc anchored on multi-walled CNTs *via* π–π interactions (Fig. 14g) exhibited high CO selectivity (FE > 90%) (Fig. 14h and i) and long-term stability in aqueous $KHCO_3$ electrolyte, with performance further enhanced by electron-withdrawing cyano substituents that promoted more favorable Co(I) formation and faster electron transfer. Beyond tuning molecular electronics, catalyst support interactions have also been shown to influence product distribution. Shen *et al.*[135] demonstrated that cobalt protoporphyrin

Open Access Article. Published on 07 mai 2025. Downloaded on 23.5.2026 05:53:41.
This article is licensed under a Creative Commons Attribution-NonCommercial 3.0 Unported Licence.

immobilized on pyrolytic graphite enables the formation of both CO and CH_4 in acidic media, and importantly, the product selectivity was highly dependent on pH, with lower pH favoring methane and higher pH favoring CO, due to the different stabilization mechanisms of reaction intermediates. More recently, Su *et al.*[136] highlighted the critical role of support-induced strain by showing that single-walled CNTs (SWCNTs), due to their high curvature, distort the CoPc molecular structure in a way that enhances CO binding and enables deeper reduction to methanol. This curvature-driven modulation led to a striking increase in methanol selectivity, achieving a FE of 53.4%, compared to just 13.9% on larger-diameter CNTs.

5.3 Graphene analogs

In addition to conventional graphene-based materials as electrocatalysts for CO_2 reduction, emerging graphene analogs, especially 2D monoelemental materials, have gained increasing attention due to their unique properties compared to traditional CO_2 electrocatalysts.[137] One of the most prominent features of these 2D monoelemental materials is their atomic thickness, which offers distinct benefits over bulk materials, including a higher density of active sites and unique electronic properties due to their reduced dimensionality. This enables enhanced catalytic performance for CO_2 reduction reactions, as the altered atomic arrangements in the 2D monolayer promote more efficient electron transfer and reaction kinetics.[138] For instance, bulk and nanoparticle forms of metals such as Sn and Bi suffer from higher overpotentials and lower current densities for electrochemical CO_2 reduction,[139–141] while their 2D monoelemental structures exhibit distinct catalytic CO_2RR.[62]

Yang *et al.*[62] demonstrated for the first time that free-standing monolayer bismuthene, synthesized through a simple and scalable wet chemical process, serves as an efficient catalyst for the electrochemical reduction of CO_2 to formate with outstanding selectivity and stability. The bismuthene catalyst achieved a FE of 99% at −580 mV *vs.* RHE (Fig. 15a), with an onset potential of less than 90 mV and stable performance over 75 hours without degradation. DFT

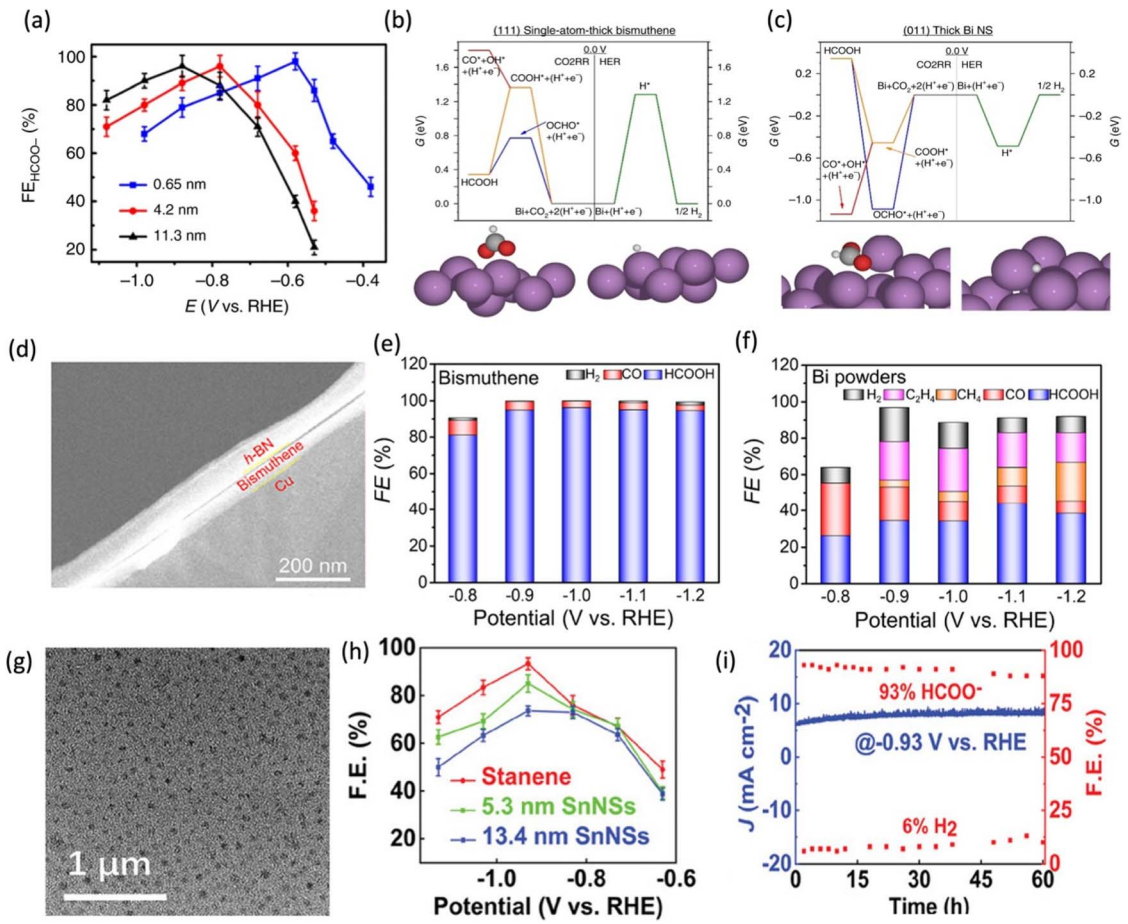

Fig. 15 Graphene analogs for eCO_2RR (a) FEs for formate *vs.* applied potential for Bi nanosheets with different thicknesses. (b) Free energy diagrams for CO_2RR and HER on (111) single-atom-thick bismuthene and (c) (011) thick Bi nanosheets at 0.0 V. HER is represented in green, CO_2RR through OCHO* and COOH* in blue and orange, respectively, and the state of CO* + OH* in red. Adapted with permission from ref. 62 Copyright 2020, Springer Nature. (d) TEM images of sandwiched bismuthene nanoflakes. (e) FEs for bismuthene nanoflakes and (f) Bi powders *vs.* applied potential within 2 hours. Adapted with permission from ref. 142 Copyright 2023, American Chemical Society. (g) TEM image of stanine. (h) FEs for formate *vs.* applied potential for Sn nanosheets with different thicknesses. (i) Stability test of stanene at −0.93 V *versus* RHE and corresponding FEs for $HCOO^-$ and H_2. Adapted with permission from ref. 143 Copyright 2024, Wiley.

© 2025 The Author(s). Published by the Royal Society of Chemistry

Open Access Article. Published on 07 mai 2025. Downloaded on 23.5.2026 05:53:41.
This article is licensed under a Creative Commons Attribution-NonCommercial 3.0 Unported Licence.

calculations ascribed the high performance to the structure-sensitive nature of CO_2 reduction on bismuthene, where the (111) facet of atomically thin nanosheets promotes selective formate production *via* an OCHO*-mediated pathway and suppresses HER due to a high overpotential (Fig. 15b). In contrast, thicker bismuth nanosheets exposing the (011) facet bind intermediates too strongly, leading to surface poisoning, which explains their lower activity and stability (Fig. 15c). These findings demonstrate bismuthene's potential as a scalable, durable, and cost-effective electrocatalyst for sustainable CO_2 utilization. However, one major limitation arises from the dense stacking of nanosheets, which creates a compact catalyst layer and restricts access to active sites, thereby limiting current output. This challenge was addressed by incorporating inert carbon black into the catalyst structure. The additive effectively inhibits nanosheet restacking, thereby improving mass transport and expanding the electrochemically active surface area. This strategy offers a promising pathway for developing composite catalyst architectures that enhance both scalability and performance in eCO_2RR.

In addition, growing high-quality 2D bismuthene in bismuthene-based catalysts remains challenging due to its high surface energy and strong interactions with metal substrates, which often cause structural distortion or aggregation into nanospheres. To address this, Hu *et al.*[142] developed a sandwiched epitaxy approach using a top hexagonal boron nitride layer on Cu foil to suppress Bi–Cu interactions and stabilize the 2D hexagonal bismuthene structure during growth. Their work demonstrated that single-crystalline hexagonal bismuthene (Fig. 15d), synthesized *via* a sandwiched epitaxy growth, exhibits excellent performance as an electrocatalyst for the selective reduction of CO_2 to formate at remarkably low overpotentials. Utilizing a CO_2-saturated 0.1 M $KHCO_3$ solution, the catalyst achieved an ultrahigh FE of 96.3% for formate production at −1.0 V *versus* RHE. In contrast, Bi powder failed to selectively produce formate, resulting in a mixture of C1 and C2 products and H_2 (Fig. 15e and f). Compared to Bi powders, bismuthene nanoflakes exhibited superior performance for formate production, achieving a higher current density and lower onset potential for the eCO_2RR. The Tafel slope for bismuthene nanoflakes (352 mV dec^{-1}) was lower than that of Bi powders (371 mV dec^{-1}), suggesting enhanced reaction kinetics. Despite having a smaller electrochemically active surface area (ECSA) than Bi powders (0.57 mF cm^{-2}), the bismuthene nanoflakes (0.34 mF cm^{-2}) demonstrated enhanced selectivity, attributed to their 2D nanostructure, which contains abundant active edge sites that effectively stabilize *OCHO intermediates, thereby reducing the occurrence of competing reactions. In addition, it was found that encapsulation by the hexagonal boron nitride layer not only prevented structural degradation but also enhanced electron transfer and stabilized reaction intermediates. This study suggests extending this encapsulation approach to synthesize other 2D materials with high surface energy, although scalability remain to be explored.

Moreover, free-standing stanine (Fig. 15g), synthesized by Mei *et al.*[143] using a bottom-up approach through a simple wet chemical method with scalable production potential, was shown to effectively catalyze the electrochemical reduction of CO_2 to formate in an aqueous solution. Using a CO_2-saturated 0.5 M $KHCO_3$ electrolyte (Fig. 15h), the stanene catalyst achieved a high FE of 93% at −0.93 V *versus* RHE with excellent stability over 60 hours (Fig. 15i). The superior performance was attributed to the high density of active edge sites on the Sn (100) step, as confirmed by DFT calculations and *in situ* Mössbauer spectroscopy. These results highlight stanene as a promising, scalable, and efficient electrocatalyst for sustainable CO_2 utilization.

6 Summary and outlook

The eCO_2RR is a valuable process for advancing sustainable development. Over the past few years, materials for ECR have undergone significant advancements, largely driven by the limitations of traditional metal-based catalysts. Graphene-based materials have emerged as a promising class of electrocatalysts for CO_2 reduction as an alternative to commercial metal catalysts. This is due to their unique structural versatility and exceptional properties, which enable superior catalytic performance. In this review, we highlight graphene-based electrocatalysts as sustainable alternatives for ECR. Graphene-based materials serve diverse roles in eCO_2RR, functioning as metal-free catalysts through heteroatom doping, as well as in combination with metals ranging from single atoms to nanoparticles and clusters. Furthermore, we provide an overview of emerging catalysts, including advanced graphene analog materials. Table 2 illustrates the recent advancements in the development of graphene-based electrocatalysts for CO_2 reduction. Despite the advantages of carbon-based catalysts and the notable progress made over the past decade, several constraints still hinder their industrial applicability.

(1) The controlled synthesis of graphene-based materials with a desired structure is essential for efficient eCO_2RR. Even minor defects, such as metal impurities or vacancies introduced during the graphene manufacturing process, can significantly influence catalytic performance. Additionally, achieving reproducible control over doping and obtaining a specific composition of heteroatom doping remains a significant challenge. For instance, in N-doped carbon materials used as catalysts for eCO_2RR, the catalytic activity is primarily attributed to active sites originating from pyridinic nitrogen, which tends to localize at the edges of carbon structures. However, precise manipulation of the types and distribution of heteroatom functionalities that enhance catalytic performance continues to be a complex task.

(2) While graphene-based catalysts exhibit promising performance for C_1 products, often rivaling or surpassing noble metals, their efficiency in producing C_{2+} products remains significantly lower than that of copper-based catalysts. Although some carbon-based materials have shown the ability to produce C_{2+} products, their partial current densities typically fall below practical thresholds resulting in limited production rates. This highlights an ongoing challenge in improving the catalytic performance of graphene-based materials for multi-carbon product synthesis.

Open Access Article. Published on 07 maí 2025. Downloaded on 23.5.2026 05:53:41.
This article is licensed under a Creative Commons Attribution-NonCommercial 3.0 Unported Licence.

Table 2 Summary of graphene-based catalysts for electrocatalytic CO2 reduction

Catalyst	Main product (FE)	Potential (V *vs.* RHE)	Current density (mA cm^{-2})	Stability	Electrolyte	Cell type	Ref.
N-doped graphene							
N-CNF	CO (98%)	−0.57 *vs.* SHE	1.3	9 h	$EMIMBF_4$	H-cell	144
N-graphene foam	CO (85%)	−0.47	1.8	5 h	0.1 M $KHCO_3$	H-cell	145
N-CNTs	CO (85%)	−0.9	5.8	60 h	0.5 M $NaHCO_3$	H-cell	146
g-C_3N_4-MWCNTs	CO (60%)	−0.75	−1.02	50 h	0.1 M $KHCO_3$	H-cell	147
N-graphene sheet	$HCOO^-$ (73%)	−0.84	7.5	12 h	0.5 M $NaHCO_3$	H-cell	148
N-graphene like carbon	CH_4 (93.5%)	−1.40	1.42	5 h	$[Bmim]BF_4$	H-cell	149
Reduced oxidized-GQDs	CH_4 (70%)	−0.9	200	10 h	1.0 M KOH	Flow cell	150
N-diamond	CH_3COO^- (91.8%)	−1.0	—	3 h	0.5 M $NaHCO_3$	H-cell	18
N-functionalized GO	C_2H_5OH (37%)	−0.4	0.745	—	0.1 M $KHCO_3$	H-cell	151
N-mesoporous carbon	C_2H_5OH (77%)	−0.56	—	6 h	0.1 M $KHCO_3$	H-cell	87
Other metal free heteroatom doped graphene							
P-OLC	CO (81%)	−0.9	4.9	27 h	0.1 M $NaHCO_3$	H-cell	152
B-diamond	HCHO (74%)	−1.7 Ag/Ag^+	—	20 h	0.1 M CH_3OH (TBAP)	H-cell	153
B-diamond	HCOO-(94.7%)	—	2	24 h	0.5 M KCl	Flow cell	86
Co-doped graphene							
N,S-NCF	CO (94%)	−0.7	103	36 h	0.1 M $KHCO_3$	H-cell	13
N,S-carbon Nanoweb	CO (93.4%)	−0.6	5.93	20 h	0.1 M $KHCO_3$	H-cell	14
N,P-mesoporous carbon	CO (100%)	−0.65	8	7 h	0.5 M $NaHCO_3$	H-cell	17
BN═C	CH_4 (68%)	−0.5	1	12 h	0.1 M $KHCO_3$	H-cell	154
B,N-nanodiamond	C_2H_5OH (93.2%)	−1.00	—	3 h	0.1 M $KHCO_3$	H-cell	155
Single atom supported on graphene							
Ni-NrGO	CO (97%)	−0.8	42	—	0.5 M $KHCO_3$	H-cell	156
Zn-NG	CO (91%)	−0.8	11.2	15 h	0.5 M $KHCO_3$	H-cell	157
Ni-NG	CO (95%)	−0.5	—	20 h	0.1 M $KHCO_3$	H-cell	158
Fe-NG	CO (80%)	−0.60	—	10 h	0.1 M $KHCO_3$	H-cell	159
Cu–N_4–NG	CO (80.6%)	−1.0	—	—	0.1 M $KHCO_3$	H-cell	160
Ni–N-MEGO	CO (92.1%)	−0.7	26.8	21 h	0.1 M $KHCO_3$	H-cell	161
Sb-graphene	HCOOH	−1.06	—	12 h	0.1 M $NaHCO_3$	H-cell	162
Bi—rGO	HCOOH	−0.57	—	30 h	0.5 M $KHCO_3$	H-cell	163
Cu–CD	CH_4 (78%)	−1.14	40	6 h	0.5 M $KHCO_3$	H-cell	75
Dual Cu SAC	C_{2+} (91%)	−1.66	90	—	0.1 M $KHCO_3$	H-cell	164
Cu–N–C-800	C_2H_4 (24.8%)	−1.4	6.84	10 h	0.1 M $KHCO_3$	H-cell	165
$Cu_{0.5}NC$	Ethanol (55%)	−1.2	16.2	—	0.1 M $CsHCO_3$	H-cell	102
Cu–SA/NPC	Acetone (36.7%)	−0.36	—	5 cycles	0.1 M $KHCO_3$	H-cell	104
Graphene-metal composite							
Bi-rGO	HCOOH (92.1%)	−0.97	28.1	30 h	0.5 M $KHCO_3$	H-cell	163
Sb NS-G	$HCOO^-$ (88.5%)	−1.0	7.5	12 h	0.5 M $NaHCO_3$	H-cell	162
Cu *Pc*_CNT	CH_4 (66%)	−1.06	13	—	0.5 M $KHCO_3$	H-cell	166
Cu_2O NCS	C_2H_4 (24.7%)	−1.3	—	4 h	0.1 M $KHCO_3$	H-cell	167
Cu NPs-N,B-graphene	C_2H_5OH (58%)	−1.0	20.4	24 h	0.5 M $KHCO_3$	H-cell	168
Co_3O_4 nanocrystals-rGO	C_2H_5OH (45.9%) C_2H_4 (28.8%)	−0.4	3.2	5 h	0.5 M $KHCO_3$	H-cell	169
Cu–Cu_2O-CeO_x-rgo	C_{2+} products (74.5%)	−0.9	230	5 h	2 M KOH	Flow cell	170
Graphene encapsulated metals							
In_2O_3 ⊃ NC@GO	$HCOO^-$ (91.2)	−0.8	40.4	10 h	0.5 M $KHCO_3$	H-cell	171
Sn quantum Sheets@Graphene	HCOOH (85%)	−1.8 V s SCE	21.1	50 h	0.5 M $NaHCO_3$	H-cell	172
Cu_2O/Cu@C/NG	HCOOH (82.1 ± 1.2%)	−0.78	—	30 h	0.1 M $KHCO_3$	H-cell	
Graphene analogs							
Bismuthene with Bi–O bond	HCOOH (84.5%)	−0.9	41.5	12 h	0.5 M $KHCO_3$	H-cell	173
Few layer bismuthene	HCOOH (96.9%)	−0.88	419.4	45 h	1 M KOH	Flow cell	174

(3) Understanding the origin of active sites and the reaction mechanism in graphene-based catalysts remains a significant challenge due to their structural complexity, the presence of multiple reaction pathways, and the rapid kinetics associated with eCO_2RR. Thus, efforts should focus on combining theoretical simulations with advanced *in situ*/*operando* techniques

© 2025 The Author(s). Published by the Royal Society of Chemistry

Open Access Article. Published on 07 maí 2025. Downloaded on 23.5.2026 05:53:41.
This article is licensed under a Creative Commons Attribution-NonCommercial 3.0 Unported Licence.

to elucidate the reaction mechanisms at the molecular level, providing deeper insights into the nature of active sites and the overall catalytic process. Such an understanding is vital for enhancing the performance of graphene-based catalysts.

(4) For practical implementation of eCO_2RR, it is essential to improve the stability of graphene-based catalysts for over 2000 hours at high current densities. Currently, most existing graphene-based catalysts only exhibit stability of less than 50 h, which falls significantly short of the durability required for industrial applications, making long-term stable operation a critical challenge for advancing the industrial application of eCO_2RR.

(5) The discovery of catalysis for electrochemical processes has greatly benefited from the integration of machine learning (ML) techniques. ML algorithms enable the analysis of vast datasets to identify trends and predict optimal doping configurations and composite designs. High-throughput computational screening, driven by ML, can significantly accelerate the material discovery and optimization process. This approach helps design graphene catalysts with properties tailored to specific reactions.

In summary, recent research highlights a growing interest in the development of graphene-based electrocatalysts for eCO_2RR. The advancements, emerging challenges, and future perspectives on graphene-based materials, including heteroatom-doped graphene and metal-graphene composites, underline their great potential for eCO_2RR applications. Ongoing research continues to pave the way for the successful application of graphene-based catalysts as sustainable and efficient solutions in CO_2 reduction.

Data availability

No primary research results, software or code have been included and no new data were generated or analyzed as part of this review.

Author contributions

Wijewardena Lankamullage Hasini Amanda: conceptualization, investigation, visualization, writing (original draft, review and editing). Woo Seok Cheon: supervision, writing (review and editing). Jungwon Park: supervision. Seol-Ha Jeong: supervision. Ho Won Jang: conceptualization, writing (review and editing), supervision, funding.

Conflicts of interest

The authors declare no conflicts of interest.

Acknowledgements

This research was supported by the National Research Foundation of Korea (NRF) funded by the Ministry of Science and ICT (MSIT), South Korea (RS-2024-00421181, and RS-2024-00405016). The Inter-University Semiconductor Research Center, Institute of Engineering Research, and SOFT Foundry at Seoul National University provided research facilities for this work. This work was also supported by the KRISS (Korea Research Institute of Standards and Science) MPI Lab. Program.

References

1 S. A. Bandh and F. A. Malla, *Biofuels in Circular Economy*, 2023.
2 A. Parekh, G. Chaturvedi and A. Dutta, *Sustain. Energy Technol. Assessments*, 2023, **55**, 102942.
3 N. Bahman, M. Al-Khalifa, S. Al Baharna, Z. Abdulmohsen and E. Khan, *Rev. Environ. Sci. Biotechnol.*, 2023, **22**, 451–470.
4 A. M. Abdellah, F. Ismail, O. W. Siig, J. Yang, C. M. Andrei, L. A. DiCecco, A. Rakhsha, K. E. Salem, K. Grandfield, N. Bassim, R. Black, G. Kastlunger, L. Soleymani and D. Higgins, *Nat. Commun.*, 2024, **15**, 1–15.
5 L. Fan, C. Xia, F. Yang, J. Wang, H. Wang and Y. Lu, *Sci. Adv.*, 2020, **6**, 1–17.
6 B. Chang, H. Pang, F. Raziq, S. Wang, K. W. Huang, J. Ye and H. Zhang, *Energy Environ. Sci.*, 2023, **16**, 4714–4758.
7 J. Han, X. Bai, X. Xu, X. Bai, A. Husile, S. Zhang, L. Qi and J. Guan, *Chem. Sci.*, 2024, **15**, 7870–7907.
8 Y. Zhao, J. Raj, X. Xu, J. Jiang, J. Wu and M. Fan, *Small*, 2024, 1–28.
9 R. Paul, L. Zhu, H. Chen, J. Qu and L. Dai, *Adv. Mater.*, 2019, **31**, 1–24.
10 F. Yu, K. Deng, M. Du, W. Wang, F. Liu and D. Liang, *Carbon Capture Sci. Technol.*, 2023, **6**, 100081.
11 M. S. K. Chowdury, Y. J. Park, S. B. Park and Y. il Park, *Sustain. Mater. Technol.*, 2024, **42**, e01124.
12 M. A. Zafar, Y. Liu, S. Allende and M. V. Jacob, *Nano-Struct. Nano-Objects*, 2024, **38**, 101129.
13 H. Yang, Y. Wu, Q. Lin, L. Fan, X. Chai, Q. Zhang, J. Liu, C. He and Z. Lin, *Angew. Chem., Int. Ed.*, 2018, **57**, 15476–15480.
14 H. Han, S. Park, D. Jang, S. Lee and W. B. Kim, *ChemSusChem*, 2020, **13**, 539–547.
15 C. Chen, X. Sun, X. Yan, Y. Wu, H. Liu, Q. Zhu, B. B. A. Bediako and B. Han, *Angew. Chem., Int. Ed.*, 2020, **59**, 11123–11129.
16 F. Yang, H. Yu, X. Mao, Q. Meng, S. Chen, Q. Deng, Z. Zeng, J. Wang and S. Deng, *Chem. Eng. J.*, 2021, **425**, 131661.
17 B. Pan, X. Zhu, Y. Wu, T. Liu, X. Bi, K. Feng, N. Han, J. Zhong, J. Lu, Y. Li and Y. Li, *Adv. Sci.*, 2020, **7**, 2–7.
18 Y. Liu, S. Chen, X. Quan and H. Yu, *J. Am. Chem. Soc.*, 2015, **137**, 11631–11636.
19 F. Yang, C. Liang, H. Yu, Z. Zeng, Y. M. Lam, S. Deng and J. Wang, *Adv. Sci.*, 2022, **9**, 1–8.
20 S. M. Lee, W. S. Cheon, M. G. Lee and H. W. Jang, *Small Struct.*, 2023, **4**(6), 2200236.
21 Z. Sun, T. Ma, H. Tao, Q. Fan and B. Han, *Chem*, 2017, **3**, 560–587.
22 J. Zhang, J. Ding, Y. Liu, C. Su, H. Yang, Y. Huang and B. Liu, *Joule*, 2023, **7**(8), 1700–1744.
23 Y. Ma, J. Yu, M. Sun, B. Chen, X. Zhou, C. Ye, Z. Guan, W. Guo, G. Wang, S. Lu, D. Xia, Y. Wang, Z. He, L. Zheng,

Open Access Article. Published on 07 maí 2025. Downloaded on 23.5.2026 05:53:41.
This article is licensed under a Creative Commons Attribution-NonCommercial 3.0 Unported Licence.

Q. Yun, L. Wang, J. Zhou, P. Lu, J. Yin, Y. Zhao, Z. Luo, L. Zhai, L. Liao, Z. Zhu, R. Ye, Y. Chen, Y. Lu, S. Xi, B. Huang, C. S. Lee and Z. Fan, *Adv. Mater.*, 2022, **34**, 1–9.
24 X. G. Zhang, S. Feng, C. Zhan, D. Y. Wu, Y. Zhao and Z. Q. Tian, *J. Phys. Chem. Lett.*, 2020, **11**, 6593–6599.
25 H. Q. Liang, T. Beweries, R. Francke and M. Beller, *Angew. Chem., Int. Ed.*, 2022, **61**(19), e202200723.
26 Y. Hori, A. Murata and R. Takahashi, *J. Chem. Soc., Faraday Trans. 1*, 1989, **85**, 2309–2326.
27 A. J. Medford, A. Vojvodic, J. S. Hummelshøj, J. Voss, F. Abild-Pedersen, F. Studt, T. Bligaard, A. Nilsson and J. K. Nørskov, *J. Catal.*, 2015, **328**, 36–42.
28 A. K. Geim and K. S. Novoselov, *Nat. Mater.*, 2007, **6**, 183–191.
29 Y. Sun, D. Song, J. Yu, J. Zhu, J. Liu, R. Chen, Q. Liu, P. Liu and J. Wang, *Surf. Sci. Technol.*, 2023, **1**, 1–14.
30 A. E. Adetayo, T. N. Ahmed, A. Zakhidov and G. W. Beall, *Adv. Opt. Mater.*, 2021, **9**, 1–23.
31 L. Wang and J. Choi, *Micro Nano Syst. Lett.*, 2022, **10**, 17.
32 M. K. Fathy, A. H. Zaki, H. A. Shawkey and H. R. Tantawy, *Trans. Electr. Electron. Mater.*, 2024, 732–744.
33 D. D. Zhu, J. L. Liu and S. Z. Qiao, *Adv. Mater.*, 2016, **28**, 3423–3452.
34 R. Kumar, S. Sahoo, E. Joanni, R. K. Singh, K. Maegawa, W. K. Tan, G. Kawamura, K. K. Kar and A. Matsuda, *Mater. Today*, 2020, **39**, 47–65.
35 X. Li, L. Fan, Z. Li, K. Wang, M. Zhong, J. Wei, D. Wu and H. Zhu, *Adv. Energy Mater.*, 2012, **2**, 425–429.
36 Y. Du, X. Meng, Z. Wang, X. Zhao and J. Qiu, *Acta Phys.-Chim. Sin.*, 2021, **38**, 1–17.
37 H. M. Jeong, J. W. Lee, W. H. Shin, Y. J. Choi, H. J. Shin, J. K. Kang and J. W. Choi, *Nano Lett.*, 2011, **11**, 2472–2477.
38 X. F. Li, K. Y. Lian, L. Liu, Y. Wu, Q. Qiu, J. Jiang, M. Deng and Y. Luo, *Sci. Rep.*, 2016, **6**, 1–10.
39 Z. Zhang, L. Yu, Y. Tu, R. Chen, L. Wu, J. Zhu and D. Deng, *Cell Reports Phys. Sci.*, 2020, **1**, 100145.
40 X. Duan, J. Xu, Z. Wei, J. Ma, S. Guo, S. Wang, H. Liu and S. Dou, *Adv. Mater.*, 2017, **29**, 1–20.
41 T. Ma, Q. Fan, X. Li, J. Qiu, T. Wu and Z. Sun, *J. CO_2 Util.*, 2019, **30**, 168–182.
42 L. Zhang, J. Niu, M. Li and Z. Xia, *J. Phys. Chem. C*, 2014, **118**, 3545–3553.
43 A. Kumar, M. Ubaidullah, P. V. Pham and R. K. Gupta, *Chem. Eng. J.*, 2024, **499**, 156664.
44 M. B. Burkholder, F. B. A. Rahman, E. H. Chandler, J. R. Regalbuto, B. F. Gupton and J. M. M. Tengco, *Carbon Trends*, 2022, **9**, 100196.
45 K. S. M. Manimehalai, S. B. Venkatesh and T. T. Subash, *Ionics*, 2025, 1467–1481.
46 J. Yan, F. Wang, S. Yin, J. Zhang and W. Jiang, *Rare Met.*, 2025, **44**, 2239–2267.
47 K. M. Yam, N. Guo, Z. Jiang, S. Li and C. Zhang, *Catalysts*, 2020, **10**(1), 53.
48 X. Tong, M. Cherif, G. Zhang, X. Zhan, J. Ma, A. Almesrati, F. Vidal, Y. Song, J. P. Claverie and S. Sun, *ACS Appl. Mater. Interfaces*, 2021, **13**, 30512–30523.
49 H. Song, M. Wu, Z. Tang, J. S. Tse, B. Yang and S. Lu, *Angew. Chem., Int. Ed.*, 2021, **60**, 7234–7244.
50 X. Liu, C. Z. Wang, M. Hupalo, W. C. Lu, M. C. Tringides, Y. X. Yao and K. M. Ho, *Phys. Chem. Chem. Phys.*, 2012, **14**, 9157–9166.
51 Y. Tang, Z. Yang and X. Dai, *J. Chem. Phys.*, 2011, **135**(22), 224704.
52 Z. Ning, Z. Chen, X. Du, R. Ran, W. Dong and C. Chen, *J. Supercond. Nov. Magn.*, 2014, **27**, 115–120.
53 Y. Zhou, G. Gao, Y. Li, W. Chu and L. W. Wang, *Phys. Chem. Chem. Phys.*, 2019, **21**, 3024–3032.
54 Y. Cheng, S. Zhao, H. Li, S. He, J. P. Veder, B. Johannessen, J. Xiao, S. Lu, J. Pan, M. F. Chisholm, S. Z. Yang, C. Liu, J. G. Chen and S. P. Jiang, *Appl. Catal., B*, 2019, **243**, 294–303.
55 H. Y. Zhuo, X. Zhang, J. X. Liang, Q. Yu, H. Xiao and J. Li, *Chem. Rev.*, 2020, **120**, 12315–12341.
56 M. Li, H. Wang, W. Luo, P. C. Sherrell, J. Chen and J. Yang, *Adv. Mater.*, 2020, **32**, 1–24.
57 A. K. Singh and S. P. Singh, *Micro Nano Syst. Lett.*, 2023, **11**, 20.
58 Y. S. Ye, M. Y. Cheng, X. L. Xie, J. Rick, Y. J. Huang, F. C. Chang and B. J. Hwang, *J. Power Sources*, 2013, **239**, 424–432.
59 P. Yang, X. Yang, W. Liu, R. Guo and Z. Yao, *Green Energy Environ.*, 2023, **8**, 1265–1278.
60 W. Tao, N. Kong, X. Ji, Y. Zhang, A. Sharma, J. Ouyang, B. Qi, J. Wang, N. Xie, C. Kang, H. Zhang, O. C. Farokhzad and J. S. Kim, *Chem. Soc. Rev.*, 2019, **48**, 2891–2912.
61 F. Pan, B. Li, W. Deng, Z. Du, Y. Gang, G. Wang and Y. Li, *Appl. Catal., B*, 2019, **252**, 240–249.
62 F. Yang, A. O. Elnabawy, R. Schimmenti, P. Song, J. Wang, Z. Peng, S. Yao, R. Deng, S. Song, Y. Lin, M. Mavrikakis and W. Xu, *Nat. Commun.*, 2020, **11**, 1088.
63 F. Liu and Z. Fan, *Chem. Soc. Rev.*, 2023, **52**, 1723–1772.
64 S. Abdullah, S. Hussain and M. Liaquat, *Dialogue Soc. Sci. Rev.*, 2025, **3**(2), 167–185.
65 X. Du Liang, N. Tian, S. N. Hu, Z. Y. Zhou and S. G. Sun, *Mater. Reports Energy*, 2023, **3**, 100191.
66 L. Chen, X. Ding, Z. Wang, S. Xu, Q. Jiang, C. Dun and J. J. Urban, *Surf. Sci. Technol.*, 2024, **2**, 9.
67 J. Li, W. Y. Zan, H. Kang, Z. Dong, X. Zhang, Y. Lin, Y. W. Mu, F. Zhang, X. M. Zhang and J. Gu, *Appl. Catal., B*, 2021, **298**, 120510.
68 J. Y. Kim, D. Hong, J. C. Lee, H. G. Kim, S. Lee, S. Shin, B. Kim, H. Lee, M. Kim, J. Oh, G. Do Lee, D. H. Nam and Y. C. Joo, *Nat. Commun.*, 2021, **12**, 1–11.
69 Y. Zhan, J. Huang, Z. Lin, X. Yu, D. Zeng, X. Zhang, F. Xie, W. Zhang, J. Chen and H. Meng, *Carbon NY*, 2015, **95**, 930–939.
70 Z. Zafar, Z. H. Ni, X. Wu, Z. X. Shi, H. Y. Nan, J. Bai and L. T. Sun, *Carbon NY*, 2013, **61**, 57–62.
71 G. D. Sun, Y. N. Cao, M. Z. Hu, X. H. Liang, Z. Wang, Z. J. Cai, F. Y. Shen, H. He, Z. X. Wang and K. Bin Zhou, *Carbon NY*, 2023, **214**, 118320.
72 B. Sheng, D. Cao, S. Chen, N. Zhang, J. Wang and L. Song, *Commun. Mater.*, 2025, **6**, 64.

© 2025 The Author(s). Published by the Royal Society of Chemistry

Open Access Article. Published on 07 maí 2025. Downloaded on 23.5.2026 05:53:41.
This article is licensed under a Creative Commons Attribution-NonCommercial 3.0 Unported Licence.

73 R. Zhao, Y. Wang, G. Ji, J. Zhong, F. Zhang, M. Chen, S. Tong, P. Wang, Z. Wu, B. Han and Z. Liu, *Adv. Mater.*, 2023, **35**, 1–11.
74 X. Li, S. Wang, L. Li, Y. Sun and Y. Xie, *J. Am. Chem. Soc.*, 2020, **142**, 9567–9581.
75 Y. Cai, J. Fu, Y. Zhou, Y. C. Chang, Q. Min, J. J. Zhu, Y. Lin and W. Zhu, *Nat. Commun.*, 2021, **12**, 1–9.
76 C. Wang, X. Wang, H. Ren, Y. Zhang, X. Zhou, J. Wang, Q. Guan, Y. Liu and W. Li, *Nat. Commun.*, 2023, **14**, 5108.
77 X. Ren, J. Zhao, X. Li, J. Shao, B. Pan, A. Salamé, E. Boutin, T. Groizard, S. Wang, J. Ding, X. Zhang, W. Y. Huang, W. J. Zeng, C. Liu, Y. Li, S. F. Hung, Y. Huang, M. Robert and B. Liu, *Nat. Commun.*, 2023, 3401.
78 J. Kim, T. Lee, H. D. Jung, M. Kim, J. Eo, B. Kang, H. Jung, J. Park, D. Bae, Y. Lee, S. Park, W. Kim, S. Back, Y. Lee and D. H. Nam, *Nat. Commun.*, 2024, 192.
79 F. Yang, X. Ma, W. Bin Cai, P. Song and W. Xu, *J. Am. Chem. Soc.*, 2019, **141**, 20451–20459.
80 J. Wu, R. M. Yadav, M. Liu, P. P. Sharma, C. S. Tiwary, L. Ma, X. Zou, X. Zhou, B. I. Yakobson, J. Lou and P. M. Ajayan, *ACS Nano.*, 2015, **9**(5), 5364–5371.
81 C. Ma, P. Hou, X. Wang, Z. Wang, W. Li and P. Kang, *Appl. Catal., B*, 2019, **250**, 347–354.
82 Y. Zhao, Q. Yuan, K. Sun, A. Wang, R. Xu, J. Xu, Y. Wang, M. Fan and J. Jiang, *ACS Appl. Mater. Interfaces*, 2023, **15**, 37593–37601.
83 H. Wang, J. Jia, P. Song, Q. Wang, D. Li, S. Min, C. Qian, L. Wang, Y. F. Li, C. Ma, T. Wu, J. Yuan, M. Antonietti and G. A. Ozin, *Angew. Chem., Int. Ed.*, 2017, **56**, 7847–7852.
84 J. Wu, S. Ma, J. Sun, J. I. Gold, C. Tiwary, B. Kim, L. Zhu, N. Chopra, I. N. Odeh, R. Vajtai, A. Z. Yu, R. Luo, J. Lou, G. Ding, P. J. A. Kenis and P. M. Ajayan, *Nat. Commun.*, 2016, **7**, 1–6.
85 N. Sreekanth, M. A. Nazrulla, T. V. Vineesh, K. Sailaja and K. L. Phani, *Chem. Commun.*, 2015, **51**, 16061–16064.
86 K. Natsui, H. Iwakawa, N. Ikemiya, K. Nakata and Y. Einaga, *Angew. Chem., Int. Ed.*, 2018, **57**, 2639–2643.
87 Y. Song, W. Chen, C. Zhao, S. Li, W. Wei and Y. Sun, *Angew. Chem., Int. Ed.*, 2017, **56**, 10840–10844.
88 D. Davis and Y. Sajeev, *Phys. Chem. Chem. Phys.*, 2014, **16**, 17408–17411.
89 Q. Yun, Q. Lu, X. Zhang, C. Tan and H. Zhang, *Angew. Chem., Int. Ed.*, 2018, **57**, 626–646.
90 K. Qu, Y. Zheng, Y. Jiao, X. Zhang, S. Dai and S. Z. Qiao, *Adv. Energy Mater.*, 2017, 1602068.
91 M. I. Cerrillo, C. Jiménez, M. Á. Ortiz, R. Camarillo, J. Rincón and F. Martínez, *J. Ind. Eng. Chem.*, 2023, **127**, 101–109.
92 B. Qiao, J. X. Liang, A. Wang, C. Q. Xu, J. Li, T. Zhang and J. J. Liu, *Nano Res.*, 2015, **8**, 2913–2924.
93 B. Qiao, J. Liu, Y. G. Wang, Q. Lin, X. Liu, A. Wang, J. Li, T. Zhang and J. Liu, *ACS Catal.*, 2015, **5**, 6249–6254.
94 Z. Zhang, Y. Zhu, H. Asakura, B. Zhang, J. Zhang, M. Zhou, Y. Han, T. Tanaka, A. Wang, T. Zhang and N. Yan, *Nat. Commun.*, 2017, **8**, 1–10.
95 H. Zhou, X. Yang, L. Li, X. Liu, Y. Huang, X. Pan, A. Wang, J. Li and T. Zhang, *ACS Catal.*, 2016, **6**, 1054–1061.
96 A. Wang, J. Li and T. Zhang, *Nat. Rev. Chem.*, 2018, **2**, 65–81.
97 Y. Pan, R. Lin, Y. Chen, S. Liu, W. Zhu, X. Cao, W. Chen, K. Wu, W. C. Cheong, Y. Wang, L. Zheng, J. Luo, Y. Lin, Y. Liu, C. Liu, J. Li, Q. Lu, X. Chen, D. Wang, Q. Peng, C. Chen and Y. Li, *J. Am. Chem. Soc.*, 2018, **140**, 4218–4221.
98 X. Li, W. Bi, M. Chen, Y. Sun, H. Ju, W. Yan, J. Zhu, X. Wu, W. Chu, C. Wu and Y. Xie, *J. Am. Chem. Soc.*, 2017, **139**, 14889–14892.
99 C. Jia, Q. Sun, R. Liu, G. Mao, T. Maschmeyer, J. J. Gooding, T. Zhang, L. Dai and C. Zhao, *Adv. Mater.*, 2024, 2404659.
100 H. Zhang, J. Li, S. Xi, Y. Du, X. Hai, J. Wang, H. Xu, G. Wu, J. Zhang, J. Lu and J. Wang, *Angew. Chem., Int. Ed.*, 2019, **58**, 14871–14876.
101 H. Yang, Y. Wu, G. Li, Q. Lin, Q. Hu, Q. Zhang, J. Liu and C. He, *J. Am. Chem. Soc.*, 2019, **141**, 12717–12723.
102 D. Karapinar, N. T. Huan, N. Ranjbar Sahraie, J. Li, D. Wakerley, N. Touati, S. Zanna, D. Taverna, L. H. Galvão Tizei, A. Zitolo, F. Jaouen, V. Mougel and M. Fontecave, *Angew. Chem., Int. Ed.*, 2019, **58**, 15098–15103.
103 L. Han, S. Song, M. Liu, S. Yao, Z. Liang, H. Cheng, Z. Ren, W. Liu, R. Lin, G. Qi, X. Liu, Q. Wu, J. Luo, H. L. Xin, X. Liu, Q. Wu, J. Luo and H. L. Xin, *J. Am. Chem. Soc.*, 2020, **142**, 12563–12567.
104 K. Zhao, X. Nie, H. Wang, S. Chen, X. Quan, H. Yu, W. Choi, G. Zhang, B. Kim and J. G. Chen, *Nat. Commun.*, 2020, **11**, 1–10.
105 Y. Li, W. Shan, M. J. Zachman, M. Wang, S. Hwang, H. Tabassum, J. Yang, X. Yang, S. Karakalos, Z. Feng, G. Wang and G. Wu, *Angew. Chem., Int. Ed.*, 2022, e202205632.
106 W. Ju, A. Bagger, G. P. Hao, A. S. Varela, I. Sinev, V. Bon, B. Roldan Cuenya, S. Kaskel, J. Rossmeisl and P. Strasser, *Nat. Commun.*, 2017, **8**, 1–9.
107 H. Bin Yang, S. F. Hung, S. Liu, K. Yuan, S. Miao, L. Zhang, X. Huang, H. Y. Wang, W. Cai, R. Chen, J. Gao, X. Yang, W. Chen, Y. Huang, H. M. Chen, C. M. Li, T. Zhang and B. Liu, *Nat. Energy*, 2018, **3**, 140–147.
108 X. Wang, Y. Wang, X. Sang, W. Zheng, S. Zhang, L. Shuai, B. Yang, Z. Li, J. Chen, L. Lei, N. M. Adli, M. K. H. Leung, M. Qiu, G. Wu and Y. Hou, *Angew. Chem.*, 2021, **133**, 4238–4244.
109 G. Luo, Y. Jing and Y. Li, *J. Mater. Chem. A*, 2020, **8**, 15809–15815.
110 X. Zhao, K. Zhao, Y. Liu, Y. Su, S. Chen, H. Yu and X. Quan, *ACS Catal.*, 2022, **12**, 11412–11420.
111 Q. Hao, H. xia Zhong, J. zhi Wang, K. hua Liu, J. min Yan, Z. hong Ren, N. Zhou, X. Zhao, H. Zhang, D. xue Liu, X. Liu, L. wei Chen, J. Luo and X. bo Zhang, *Nat. Synth.*, 2022, **1**, 719–728.
112 L. Zhang, J. Feng, S. Liu, X. Tan, L. Wu, S. Jia, L. Xu, X. Ma, X. Song, J. Ma, X. Sun and B. Han, *Adv. Mater.*, 2023, **35**, 1–10.
113 M. Karuppannan, Y. Kim, S. Gok, E. Lee, J. Y. Hwang, J. H. Jang, Y. H. Cho, T. Lim, Y. E. Sung and O. J. Kwon, *Energy Environ. Sci.*, 2019, **12**, 2820–2829.

Open Access Article. Published on 07 maí 2025. Downloaded on 23.5.2026 05:53:41.
This article is licensed under a Creative Commons Attribution-NonCommercial 3.0 Unported Licence.

114 Y. Zhang, P. He, D. Zhuo, J. Zhang, N. Zhang, X. Wang, G. Lin and Z. Kong, *Electron. Mater. Lett.*, 2024, **20**, 95–101.
115 V. Kumar, R. K. Mishra, L. G. Trung, P. Kumar, S. M. Mane, J. C. Shin and J. S. Gwag, *Electron. Mater. Lett.*, 2024, **20**, 414–424.
116 H. Y. Kim, J. Y. Kim and S. H. Joo, *Bull. Korean Chem. Soc.*, 2021, **42**, 724–736.
117 M. Sharma, J. H. Jang, D. Y. Shin, J. A. Kwon, D. H. Lim, D. Choi, H. Sung, J. Jang, S. Y. Lee, K. Y. Lee, H. Y. Park, N. Jung and S. J. Yoo, *Energy Environ. Sci.*, 2019, **12**, 2200–2211.
118 S. Popović, M. Smiljanić, P. Jovanovič, J. Vavra, R. Buonsanti and N. Hodnik, *Angew. Chem., Int. Ed.*, 2020, **59**, 14736–14746.
119 W. T. Osowiecki, J. J. Nussbaum, G. A. Kamat, G. Katsoukis, M. Ledendecker, H. Frei, A. T. Bell and A. P. Alivisatos, *ACS Appl. Energy Mater.*, 2019, **2**, 7744–7749.
120 Y. G. Kim, J. H. Baricuatro, A. Javier, J. M. Gregoire and M. P. Soriaga, *Langmuir*, 2014, **30**, 15053–15056.
121 J. Vavra, T. H. Shen, D. Stoian, V. Tileli and R. Buonsanti, *Angew. Chem., Int. Ed.*, 2021, **60**, 1347–1354.
122 P. Grosse, D. Gao, F. Scholten, I. Sinev, H. Mistry and B. Roldan Cuenya, *Angew. Chem.*, 2018, **130**, 6300–6305.
123 W. Drisdell, S. H. Lee, D. Lee, D. Larson, H. Li, J. Chen, S. Blair, A. Gallo, H. Zheng, C. Tassone and T. Jaramillo, *Preprint*, 2023, 1–21.
124 J. M. Yoo, H. Shin, D. Y. Chung and Y. E. Sung, *Acc. Chem. Res.*, 2022, **55**, 1278–1289.
125 V. Okatenko, A. Loiudice, M. A. Newton, D. C. Stoian, A. Blokhina, A. N. Chen, K. Rossi and R. Buonsanti, *J. Am. Chem. Soc.*, 2023, **145**, 5370–5383.
126 K. Maekawa, K. Mori, N. Suzumura, K. Honda, Y. Hirose, K. Asai, A. Uedono and M. Kojima, *Microelectron. Eng.*, 2008, **85**, 2137–2141.
127 T. Yao, W. Xia, S. Han, S. Jia, X. Dong, M. Wang, J. Jiao, D. Zhou, J. Yang, X. Xing, C. Chen, M. He, H. Wu and B. Han, *Chem. Sci.*, 2023, **14**, 14308–14315.
128 C. Xu, A. Vasileff, B. Jin, D. Wang, H. Xu, Y. Zheng and S. Z. Qiao, *Chem. Commun.*, 2020, **56**, 11275–11278.
129 J. Yuan, M. P. Yang, W. Y. Zhi, H. Wang, H. Wang and J. X. Lu, *J. CO_2 Util.*, 2019, **33**, 452–460.
130 D. C. B. Alves, R. Silva, D. Voiry, T. Asefa and M. Chhowalla, *Mater. Renew. Sustain. Energy*, 2015, **4**, 2.
131 S. Asperti, R. Hendrikx, Y. Gonzalez-Garcia and R. Kortlever, *ChemCatChem*, 2022, **14**, 1–8.
132 J. Darayen, O. Chailapakul, P. Praserthdam, J. Panpranot, D. N. Tungasmita and Y. Boonyongmaneerat, *Appl. Sci.*, 2022, 11104.
133 T. Burwell, M. Thangamuthu, G. N. Aliev, S. Ghaderzadeh, E. C. Kohlrausch, Y. Chen, W. Theis, L. T. Norman, J. A. Fernandes, E. Besley, P. Licence and A. N. Khlobystov, *Commun. Chem.*, 2024, **7**, 1–10.
134 X. Zhang, Z. Wu, X. Zhang, L. Li, Y. Li, H. Xu, X. Li, X. Yu, Z. Zhang, Y. Liang and H. Wang, *Nat. Commun.*, 2017, **8**, 1–8.
135 J. Shen, R. Kortlever, R. Kas, Y. Y. Birdja, O. Diaz-Morales, Y. Kwon, I. Ledezma-Yanez, K. J. P. Schouten, G. Mul and M. T. M. Koper, *Nat. Commun.*, 2015, 8177.
136 J. Su, C. B. Musgrave, Y. Song, L. Huang, Y. Liu, G. Li, Y. Xin, P. Xiong, M. M. J. Li, H. Wu, M. Zhu, H. M. Chen, J. Zhang, H. Shen, B. Z. Tang, M. Robert, W. A. Goddard and R. Ye, *Nat. Catal.*, 2023, **6**, 818–828.
137 N. Han, Y. Wang, H. Yang, J. Deng, J. Wu, Y. Li and Y. Li, *Nat. Commun.*, 2018, **9**, 1–8.
138 W. Yang, X. Zhang and Y. Xie, *Nano Today*, 2016, **11**, 793–816.
139 X. Yu, Y. Fautrelle, Z. Ren and X. Li, *Mater. Lett.*, 2015, **161**, 144–148.
140 B. Ávila-Bolívar, L. García-Cruz, V. Montiel and J. Solla-Gullón, *Molecules*, 2019, **24**, 1–15.
141 X. Tan, S. Jia, X. Song, X. Ma, J. Feng, L. Zhang, L. Wu, J. Du, A. Chen, Q. Zhu, X. Sun and B. Han, *Chem. Sci.*, 2023, **14**, 8214–8221.
142 Y. Hu, J. Liang, Y. Gu, S. Yang, W. Zhang, Z. Tie, J. Ma and Z. Jin, *Nano Lett.*, 2023, **23**, 10512–10521.
143 X. Mei, C. Liu, D. Zhang, J. Cao, R. Ge, J. Wang and W. Xu, *Adv. Energy Mater.*, 2024, **14**, 1–7.
144 B. Kumar, M. Asadi, D. Pisasale, S. Sinha-Ray, B. A. Rosen, R. Haasch, J. Abiade, A. L. Yarin and A. Salehi-Khojin, *Nat. Commun.*, 2013, **4**, 1–8.
145 J. Wu, M. Liu, P. P. Sharma, R. M. Yadav, L. Ma, Y. Yang, X. Zou, X. D. Zhou, R. Vajtai, B. I. Yakobson, J. Lou and P. M. Ajayan, *Nano Lett.*, 2016, **16**, 466–470.
146 J. Xu, Y. Kan, R. Huang, B. Zhang, B. Wang, K. H. Wu, Y. Lin, X. Sun, Q. Li, G. Centi and D. Su, *ChemSusChem*, 2016, **9**, 1085–1089.
147 X. Lu, T. H. Tan, Y. H. Ng and R. Amal, *Chem.–A Eur. J.*, 2016, **22**, 11991–11996.
148 H. Wang, Y. Chen, X. Hou, C. Ma and T. Tan, *Green Chem.*, 2016, **18**, 3250–3256.
149 X. Sun, X. Kang, Q. Zhu, J. Ma, G. Yang, Z. Liu and B. Han, *Chem. Sci.*, 2016, **7**, 2883–2887.
150 T. Zhang, W. Li, K. Huang, H. Guo, Z. Li, Y. Fang, R. M. Yadav, V. Shanov, P. M. Ajayan, L. Wang, C. Lian and J. Wu, *Nat. Commun.*, 2021, **12**, 1–9.
151 J. Yuan, W. Y. Zhi, L. Liu, M. P. Yang, H. Wang and J. X. Lu, *Electrochim. Acta*, 2018, **282**, 694–701.
152 T. Liu, S. Ali, Z. Lian, C. Si, D. S. Su and B. Li, *J. Mater. Chem. A*, 2018, **6**, 19998–20004.
153 K. Nakata, T. Ozaki, C. Terashima, A. Fujishima and Y. Einaga, *Angew. Chem., Int. Ed.*, 2014, **53**, 871–874.
154 B. Yuying Zhaoa, b, Q. Yuanb, M. Fana, A. O. Wanga, K. Suna, Z. Wangc and J. Jianga, *Chinese Chem. Lett.*, 2023, **34**, 108120.
155 Y. Liu, Y. Zhang, K. Cheng, X. Quan, X. Fan, Y. Su, S. Chen, H. Zhao, Y. Zhang, H. Yu and M. R. Hoffmann, *Angew. Chem., Int. Ed.*, 2017, **56**, 15607–15611.
156 H. Y. Jeong, M. Balamurugan, V. S. K. Choutipalli, J. Jo, H. Baik, V. Subramanian, M. Kim, U. Sim and K. T. Nam, *Chem.–A Eur. J.*, 2018, **24**, 18444–18454.
157 Z. Chen, K. Mou, S. Yao and L. Liu, *ChemSusChem*, 2018, **11**, 2944–2952.
158 K. Jiang, S. Siahrostami, T. Zheng, Y. Hu, S. Hwang, E. Stavitski, Y. Peng, J. Dynes, M. Gangisetty, D. Su,

© 2025 The Author(s). Published by the Royal Society of Chemistry

Open Access Article. Published on 07 maí 2025. Downloaded on 23.5.2026 05:53:41.
This article is licensed under a Creative Commons Attribution-NonCommercial 3.0 Unported Licence.

K. Attenkofer and H. Wang, *Energy Environ. Sci.*, 2018, **11**, 893–903.
159 C. Zhang, S. Yang, J. Wu, M. Liu, S. Yazdi, M. Ren, J. Sha, J. Zhong, K. Nie, A. S. Jalilov, Z. Li, H. Li, B. I. Yakobson, Q. Wu, E. Ringe, H. Xu, P. M. Ajayan and J. M. Tour, *Adv. Energy Mater.*, 2018, **8**, 1–9.
160 C. Xu, X. Zhi, A. Vasileff, D. Wang, B. Jin, Y. Jiao, Y. Zheng and S. Z. Qiao, *Small Struct.*, 2021, **2**, 1–7.
161 Y. Cheng, S. Zhao, H. Li, S. He, J. P. Veder, B. Johannessen, J. Xiao, S. Lu, J. Pan, M. F. Chisholm, S. Z. Yang, C. Liu, J. G. Chen and S. P. Jiang, *Appl. Catal., B*, 2019, **243**, 294–303.
162 F. Li, M. Xue, J. Li, X. Ma, L. Chen, X. Zhang, D. R. MacFarlane and J. Zhang, *Angew. Chem., Int. Ed.*, 2017, **56**, 14718–14722.
163 D. Wu, W. Chen, X. Wang, X. Z. Fu and J. L. Luo, *J. CO_2 Util.*, 2020, **37**, 353–359.
164 S. Li, A. Guan, C. Yang, C. Peng, X. Lv, Y. Ji, Y. Quan, Q. Wang, L. Zhang and G. Zheng, *ACS Mater. Lett.*, 2021, **3**, 1729–1737.
165 A. Guan, Z. Chen, Y. Quan, C. Peng, Z. Wang, T. K. Sham, C. Yang, Y. Ji, L. Qian, X. Xu and G. Zheng, *ACS Energy Lett.*, 2020, **5**, 1044–1053.
166 Z. Weng, Y. Wu, M. Wang, J. Jiang, K. Yang, S. Huo, X. F. Wang, Q. Ma, G. W. Brudvig, V. S. Batista, Y. Liang, Z. Feng and H. Wang, *Nat. Commun.*, 2018, **9**, 1–9.
167 H. Ning, X. Wang, W. Wang, Q. Mao, Z. Yang, Q. Zhao, Y. Song and M. Wu, *Carbon NY*, 2019, **146**, 218–223.
168 Y. Zhao, Q. Yuan, R. Xu, C. Zhang, K. Sun, A. Wang, A. Zhang, Z. Wang, J. Jiang and M. Fan, *Appl. Catal., B*, 2024, **355**, 124168.
169 S. Saha, S. Maitra, M. Chattopadhyaya, A. Sarkar, S. Haque, S. Roy and K. Kargupta, *ACS Appl. Nano Mater.*, 2022, **5**, 10369–10382.
170 Z. Zhang, X. Wang, H. Tian, H. Jiao, N. Tian, L. Bian, Y. Liu and Z. L. Wang, *J. Colloid Interface Sci.*, 2024, **661**, 966–976.
171 Y. Wang, J. Ding, J. Zhao, J. Wang, X. Han, Y. Deng and W. Hu, *J. Mater. Sci. Technol.*, 2022, **121**, 220–226.
172 F. Lei, W. Liu, Y. Sun, J. Xu, K. Liu, L. Liang, T. Yao, B. Pan, S. Wei and Y. Xie, *Nat. Commun.*, 2016, **7**, 1–8.
173 B. Ning, Q. Xu, M. Liu, H. Jiang, Y. Hu and C. Li, *Chem. Eng. Sci.*, 2022, **251**, 117409.
174 X. Wang, D. Song, C. Wang, Y. Wang, J. H. Jiang, J. Huo and Z. Li, *ACS Appl. Nano Mater.*, 2023, **6**, 17357–17363.

© 2025 The Author(s). Published by the Royal Society of Chemistry